

AD-A276 211



PART 1 OF 2



Office of Naval Research
Grant N00014-89-J-1795

2
DTIC
SELECTED
FEB 17 1994
S B D

Final Report

Noninvasive Spectral Analysis and
Beam Mapping of Focused Ultrasound

by

Walter Mayer (Principal Investigator)

Thomas Neighbors

Herbert Ruf

John Wolf

Qicao Zhu

Ultrasonics Research Laboratory
Physics Department
Georgetown University
Washington, DC 20057

January 1994

DISTRIBUTION STATEMENT A
Approved for public release
Distribution Unlimited

Reproduction in whole or in parts permitted for any purpose
of the United States Government



94-05245

DTIC QUALITY INSPECTED 2

94 2 16 104

**Best
Available
Copy**

REPORT DOCUMENTATION PAGE

Form Approved
OMB No. 0704-0188

Public reporting burden for this collection of information is estimated to average 1 hour per response, including the time for reviewing instructions, searching existing data sources, gathering and maintaining the data needed, and completing and reviewing the collection of information. Send comments regarding this burden estimate or any other aspect of this collection of information, including suggestions for reducing this burden, to Washington Headquarters Services, Directorate for Information Operations and Reports, 1215 Jefferson Davis Highway, Suite 1204, Arlington, VA 22202-4302, and to the Office of Management and Budget, Paperwork Reduction Project (0704-0188), Washington, DC 20503.

1. AGENCY USE ONLY (Leave blank)	2. REPORT DATE	3. REPORT TYPE AND DATES COVERED	
	18 January 1994	Final 01 Apr 89 - 30 Sep 93	
4. TITLE AND SUBTITLE		5. FUNDING NUMBERS	
NONINVASIVE SPECTRAL ANALYSIS AND BEAM MAPPING OF FOCUSED ULTRASOUND		PE 61153N G N00014-89-J-1795 TA 3126948	
6. AUTHOR(S)			
Walter Mayer, Thomas Neighbors, Herbert Ruf, John Wolf, and Qicao Zhu			
7. PERFORMING ORGANIZATION NAME(S) AND ADDRESS(ES)		8. PERFORMING ORGANIZATION REPORT NUMBER	
Georgetown University 37 & "O" Streets, NW Washington, DC 20057			
9. SPONSORING/MONITORING AGENCY NAME(S) AND ADDRESS(ES)		10. SPONSORING/MONITORING AGENCY REPORT NUMBER	
Office of Naval Research Physics Division ONR 312 800 North Quincy St Arlington, VA 22217-5660			
11. SUPPLEMENTARY NOTES			
12a. DISTRIBUTION/AVAILABILITY STATEMENT		12b. DISTRIBUTION CODE	
Approved for public release: Distribution unlimited			
13. ABSTRACT (Maximum 200 words)			
This is a report on the noninvasive analysis of ultrasonic fields where nonlinear distort initially sinusoidal sound fields, with the main emphasis being placed on the acousto-optic (schlieren) investigation of line-focused ultrasound propagating in water. Computational models and experimental results are presented as well as some results of phenomena related to reflection and transmission at boundaries of pulsed sound fields.			
14. SUBJECT TERMS		15. NUMBER OF PAGES	
Ultrasound (focused); ultrasound (pulsed), noninvasive method; acousto-optics; nonlinear ultrasonics.		133	
16. PRICE CODE			
17. SECURITY CLASSIFICATION OF REPORT	18. SECURITY CLASSIFICATION OF THIS PAGE	19. SECURITY CLASSIFICATION OF ABSTRACT	20. LIMITATION OF ABSTRACT
UNCLASSIFIED	UNCLASSIFIED	UNCLASSIFIED	

INTRODUCTION

The main theme of the present Grant was the noninvasive spectral analysis of ultrasonic fields where nonlinear properties of the medium of propagation cause initially sinusoidal ultrasonic waves to become distorted and thus exhibit more than one frequency component in the sound field.

There are a number of cases where such "finite amplitude effects" - as opposed to infinitesimally small amplitudes of the signal where nonlinearities can be neglected- occur. All of them are related to high amplitude waves propagating in water; the most common ones are:

- High amplitude continuous wave bounded beams,
- Ultrasonic pulses,
- Focused ultrasonic beams.

The work performed consisted primarily of theoretical and experimental analyses of the spectral contents of these three sound fields and, secondarily, of the investigation of reflection, transmission, and reradiation phenomena when such fields encounter liquid/solid interfaces, like solid plates immersed in water.

The theoretical analysis was concerned with two topics. The first was the computation model of the changes in the harmonic contents and the pressure profile of the sound signal as a function of travel distance.

(a) In the case of line focused ultrasound the theoretical sound pressure field predictions were based on a numerical solution of a differential equation describing nonlinear effects, the Khokhlov-Zabolotskaya-Kuznetsov equation. A method was found to greatly enhance the computational effectiveness of the numerical solution.

(b) In the case of pulsed ultrasound, the important factors were found to be the Fourier series, whose lowest frequency component is the pulse repetition rate, and the changes in that frequency spectrum due to nonlinear processes as the signal progresses.

The second general theoretical topic was concerned with the calculation of the acousto-optic interaction of pulsed ultrasound and monochromatic light. This interaction produces a distinctive diffraction pattern where the light intensity in the many diffraction orders is determined by the frequency spectrum of the signal. The various aspects of these two theoretical approaches will be discussed in later sections of this report.

The experimental analysis was done by using acousto-optic techniques to probe the sound fields. The advantage here is the fact that the sound field is not being disturbed by the measurement since no material object, like a hydrophone, needs to be placed in the sound field. Both diffraction order analysis and Schlieren techniques were used to verify theoretical predictions and in some cases to establish the basis for further theoretical considerations.

This report is structured according to the outline given above. The sections are separated and are preceded by individual Summary Pages. The Appendices contain listings of computational codes and/or reprints of papers which have a bearing on the main themes.

Accession For	
NTIS GRA&I	<input checked="" type="checkbox"/>
DTIG TAB	<input type="checkbox"/>
Unannounced	<input type="checkbox"/>
Justification	
By	
Distribution/	
Availability Codes	
Distr	Avail and/or Special
A-1	

Summary Page I

This section was prepared by Dr. Thomas Neighbors who has done the computational approach to the calculation of pressure profile in a line-focused ultrasonic beam. The experimental results presented in this section were obtained by Herbert Ruf. Both these authors were partially supported by the present Grant; Dr. Neighbors for a very short time as Research Associate Professor, and Dr. Ruf for most of the duration of the Grant as graduate student and later as post-doctoral fellow.

This section is entitled "Line Focused Transducers - Equations and Field Determinations." The KZK equation is stated and then used to apply to line-focused sound sources. The needed mathematical operations are indicated so the equation can be written in normalized terms.

After the focused beam boundary conditions are enumerated, the KZK equation Fourier decomposition for line focused sources is performed. The main problem is the solution of an infinite set of coupled nonlinear equations. The key steps to do this in an efficient yet reliable way are listed and the numerical solutions are discussed, concentrating on the validity of the idea of accepting "floating" boundary conditions, the flexible allocation of harmonic terms, and lastly, the convergence of the solution.

This is followed by the listing of results for concrete examples of line-focused beams, giving the initial conditions at the source. This is compared with experimental results, where the experiments are performed making use of acousto-optic methods.

This section closes with a statement of the predicted changes in the focal length of the transducer when the pressure is increased.

Line Focused Transducers

Equations and Field Determinations

Thomas Heighbors and Herbert Ruf

**Ultrasonics Research Laboratory - Physics Department
Georgetown University**

TABLE OF CONTENTS

1.0 Introduction	1
2.0 KZK Equation For Line Focused Source	2
3.0 Focused Beam Boundary Conditions	5
4.0 KZK equation Fourier decomposition for line focused source	6
5.0 KZK Equation Numerical Solution	9
5.1 "Floating" or Expanding Boundary Condition	10
5.2 Dynamic Allocation Of Harmonic Terms	13
5.3 Numerical Solution Convergence	16
6.0 KZK Line focus equation numerical predictions	18
6.1 Initial conditions	19
6.2 Peak Pressure Profile - 58.05 kPa source	19
6.3 Predicted Impact of Increased Pressure	22

Line Focus Equation Derivation

1.0 Introduction

The Khokhlov-Zabolotskaya-Kuznetsov (KZK) parabolic equation is generally used to account for nonlinearity, diffraction and attenuation in a directive, finite-amplitude sound beam¹. The KZK equation is given by:

$$\frac{\partial^2 P}{\partial z \partial t'} - \frac{c_0}{2} \nabla_{\perp}^2 P - \frac{b}{2\rho_0 c_0^3} \frac{\partial^3 P}{\partial t'^3} = \frac{\beta}{2\rho_0 c_0^3} \frac{\partial^2 P^2}{\partial t'^2} \quad (1)$$

where

- c_0 = isentropic speed of sound,
- ρ_0 = fluid density,
- β = coefficient of nonlinearity,
- t' = retarded time ($t - z/c_0$),
- t = time,
- z = on-axis distance,
- P = pressure,
- ∇_{\perp} = transverse Laplacian, and
- b = thermo-viscous loss term.

Originally Eq. 1 was derived without thermo-viscous losses by Khokhlov and Zabolotskaya. The adaption to include dissipation is due to Kuznetsov. A recent re-derivation² has shown that Eq. 1 accounts for nonlinearity, diffraction and absorption to an

equal order of magnitude. The $\nabla_1^2 P$ term corresponds to diffraction effects. In deriving Eq. 1 a well collimated beam is assumed, e.g. $ka \gg 1$ with $k = \omega/c_0$ and with a = the source radius.

The following sections outline the approach used in applying the KZK equation to a line focused radiator. Section 2 starts by outlining the modifications in the parabolic equation necessary for its initial application to the line focused radiator. Section 3 briefly outlines the change in the boundary conditions necessary when the KZK equation is used for a focused source. This is followed in section 4 by the Fourier series expansion of the modified KZK equation which results in an infinite set of coupled nonlinear differential equations for the pressure spectral terms. Section 5 takes the coupled nonlinear differential equations and discusses the computational efficiency enhancement techniques which allow their numerical solution on a desk top computer.

2.0 KZK Equation For Line Focused Source

For a geometry which considers only the $y z$ plane with z the propagation direction and y perpendicular to z , the transverse gradient can be replaced with $\partial^2 y$. This approach assumes that to first order the variations in the x direction can be ignored.

$$\frac{\partial^2 P}{\partial z \partial t'} - \frac{c_0 \partial^2 P}{2 \partial y^2} - \frac{b}{2 \rho_0 c_0^3} \frac{\partial^3 P}{\partial t'^3} = \frac{\beta}{2 \rho_0 c_0^3} \frac{\partial^2 P^2}{\partial t'^2} \quad (2)$$

If the retarded time is replaced by a normalized retarded time, i.e. $\tau = \omega t'$, then $\partial t' = \partial \tau / \omega$ and equation (2) can be rewritten as

$$\frac{\omega \partial^2 P}{\partial z \partial \tau} - \frac{c_0 \partial^2 P}{2 \partial y^2} - \frac{b \omega^3}{2 \rho_0 c_0^3} \frac{\partial^3 P}{\partial \tau^3} - \frac{\beta \omega^2}{2 \rho_0 c_0^3} \frac{\partial^2 P^2}{\partial \tau^2} \quad (3)$$

The geometry used in applying the KZK equation to focused sound propagation is in Figure 1. The acoustic field originates at a concave source, of transverse diameter $2a$, and propagates in the z direction towards the geometric focus which is nominally located at the source radius of curvature d .

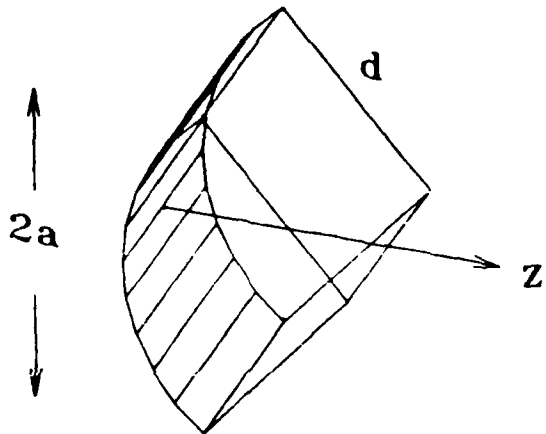


Figure 1. Line Focused Radiator Dimensions

To simplify equation (3), renormalize the on-axis distance, z , to the radius of curvature of the line focus radiator, d , with the new distance parameter being $\sigma = z/d$.

$$\frac{\omega}{d} \frac{\partial^2 P}{\partial \sigma \partial \tau} - \frac{c_0 \partial^2 P}{2 \partial y^2} - \frac{b \omega^3}{2 \rho_0 c_0^3} \frac{\partial^3 P}{\partial \tau^3} = \frac{\beta \omega^2}{2 \rho_0 c_0^3} \frac{\partial^2 P^2}{\partial \tau^2} \quad (4)$$

Equation (4) can be reduced even further by normalizing the transverse coordinate to the radiator's transverse radius a , as shown in Figure 1. With the new transverse coordinate $r = y/a$, equation (4) becomes.

$$\frac{\omega}{c_0} \frac{\partial^2 F}{\partial \sigma \partial \tau} - \frac{c_0}{2a^2} \frac{\partial^2 P}{\partial r^2} - \frac{b\omega^3}{2\rho_0 c_0^3} \frac{\partial^3 P}{\partial \tau^3} - \frac{\beta \omega^2}{2\rho_0 c_0^3} \frac{\partial^2 P^2}{\partial \tau^2} \quad (5)$$

At this point, we can convert to a normalized pressure by dividing P by the on-axis peak pressure at the surface of the line focused radiator, p_0 , e.g. $p = P/p_0$.

$$\frac{\omega p_0}{d} \frac{\partial^2 p}{\partial \sigma \partial \tau} - \frac{c_0 p_0}{2a^2} \frac{\partial^2 p}{\partial r^2} - \frac{b\omega^3 p_0}{2\rho_0 c_0^3} \frac{\partial^3 p}{\partial \tau^3} = \frac{\beta \omega^2 p_0^2}{2\rho_0 c_0^3} \frac{\partial^2 p^2}{\partial \tau^2} \quad (6)$$

Multiply by $d/\omega p_0$ and we have

$$\frac{\partial^2 p}{\partial \sigma \partial \tau} - \frac{c_0 d}{2\omega a^2} \frac{\partial^2 p}{\partial r^2} - \frac{b\omega^2 d}{2\rho_0 c_0^3} \frac{\partial^3 p}{\partial \tau^3} = \frac{\beta \omega p_0 d}{2\rho_0 c_0^3} \frac{\partial^2 p^2}{\partial \tau^2} \quad (7)$$

Equation (7) can be simplified by using the standard definitions of the Rayleigh distance, z_0 , and the discontinuity distance, l_d given in equations (8) and (9).

$$z_0 = \frac{\omega a^2}{2c_0} \quad (8)$$

and

$$l_d = \frac{\rho_0 c_0^3}{\beta \omega p_0} \quad (9)$$

Equation (10) is the result of the substitution.

$$\frac{\partial^2 p}{\partial \sigma \partial \tau} - \frac{d}{4z_0} \frac{\partial^2 p}{\partial r^2} - \frac{b\omega^2 d}{2\rho_0 c_0^3} \frac{\partial^3 p}{\partial \tau^3} = \frac{d}{2L_d} \frac{\partial^2 p^2}{\partial \tau^2} \quad (10)$$

Identifying the last set of constants as α , the thermal viscous loss coefficient and making the substitution shown below for αd yields equation (12).

$$\alpha d = \frac{bd\omega^2}{2\rho_0 c_0^3} \quad (11)$$

Then we have the line focus KZK equation in normalized terms.

$$\frac{\partial^2 p}{\partial \sigma \partial \tau} - \frac{d}{4z_0} \frac{\partial^2 p}{\partial r^2} - \alpha d \frac{\partial^3 p}{\partial \tau^3} = \frac{d}{2L_d} \frac{\partial^2 p^2}{\partial \tau^2} \quad (12)$$

3.0 Focused Beam Boundary Conditions

To effect a solution of Eq. 12 it is necessary to specify the initial pressure distribution $p(y, z, t)$ at $z = 0$. The standard approach for specifying the initial condition uses the quasi-optical approximation which modifies the amplitude and phase of the pressure distribution in the xy plane at $z = 0$ to produce the amplitude and phase distribution that would occur at the surface of the concave source. Figures 2a and 2b illustrate the phase and amplitude adjustment, respectively. The phase adjustment shown in Figure 2a is $k \cdot dx$ where $k = 2\pi/\lambda$ and dx is the distance that would have to be propagated from the xy plane to the curved surface.

The amplitude correction requires a bit more explanation as shown in Fig 2b. Since the initial pressure distribution in each elementary radial segment along the y axis, dy , over

the interval $[0,a]$ represents the pressure on a segment of the curved surface, the required increase in the normalized pressure at $z = 0$ is given by $D \cdot d\theta/dy$. As shown in Figs. 2a and 2b, θ is the angle measured from the z axis and D is the source radius of curvature.

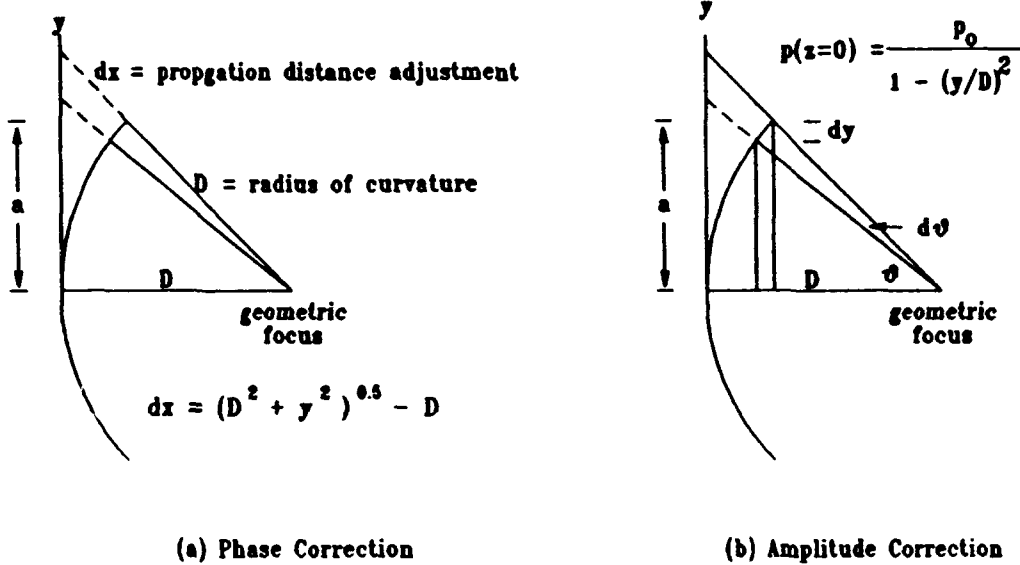


Figure 2. Initial Pressure Phase and Amplitude Adjustment

4.0 KZK equation Fourier decomposition for line focused source

Since a general analytic solution of the KZK equation has not been found to date³, the equation is usually solved by a number of approximations and numerical techniques. The approach used here has been adapted from the numerical solution initially developed by Aanonsen⁴, enhanced by Hart and Hamilton⁵, and revised by Neighbors and Bjorno. The numerical approach allows solutions within a range of assumptions which are not too restrictive.

Assume the initial pressure at $\sigma = 0$ can be represented as a periodic function of the form

$$p = \sum_{n=-\infty}^{\infty} p_n e^{jnr} \quad (13)$$

with

$$p_n = \frac{1}{\pi} \int_{-\pi}^{\pi} p(\tau) e^{-jnr} d\tau \quad (14)$$

Now if we substitute Eq. 13 into Eq. 12 we have the following set of coupled nonlinear differential equations in terms of the Fourier components:

$$\begin{aligned} & \sum_{n=-\infty}^{\infty} \left[jn \frac{\partial p_n}{\partial \sigma} - \frac{d}{4z_0} \frac{\partial^2 p_n}{\partial r^2} - \alpha d(jn)^3 p_n \right] e^{jnr} \\ &= \frac{d}{2l_d} \frac{\partial^2}{\partial \tau^2} \left[\sum_{n=-\infty}^{\infty} \sum_{m=-\infty}^{\infty} p_n e^{jnr} p_m e^{jmr} \right] \end{aligned} \quad (15)$$

To convert Eq 15 into a set of coupled partial differential equations in terms of p_n requires a transformation of the right hand side of Eq 15. First, let $k = n + m$, then we have

$$\sum_{n=-\infty}^{\infty} \sum_{m=-\infty}^{\infty} p_n e^{jnr} p_m e^{jmr} = \sum_{n=-\infty}^{\infty} \sum_{k=-\infty}^{\infty} p_n p_k e^{jkr}$$

Rotating the indices and letting $k \rightarrow n$ and $n \rightarrow k$ yields

$$\sum_{n=-\infty}^{\infty} \sum_{m=-\infty}^{\infty} p_n e^{jnr} p_m e^{jmr} = \sum_{n=-\infty}^{\infty} \left[\sum_{k=-\infty}^{\infty} p_k p_{n-k} \right] e^{jnr} \quad (17)$$

The products of e^{jnr} now become an infinite set of coupled partial differential

equations for p_n of the form

$$jn \frac{\partial p_n}{\partial \sigma} - \frac{d}{4z_0} \frac{\partial^2 p_n}{\partial r^2} - \alpha d(jn)^3 p_n = \frac{d(jn)^2}{2I_d} \sum_{k=-\infty}^{\infty} p_k p_{n-k} \quad (18)$$

Since the initial pressure is real, $p_n = p_n^*$ where the * denotes the complex conjugate. Using this property and manipulating the summation indices yields equation (19) which is an infinite set of coupled partial differential equations for the Fourier amplitude coefficients p_n .

$$jn \frac{\partial p_n}{\partial \sigma} - \frac{d}{4z_0} \frac{\partial^2 p_n}{\partial r^2} - \alpha d(jn)^3 p_n = \frac{d(jn)^2}{2I_d} \left[\sum_{k=1}^{n-1} p_k p_{n-k} + 2 \sum_{k=n+1}^{\infty} p_k p_{k-n}^* \right] \quad (19)$$

The standard approach for solving the infinite set of coupled nonlinear equations truncates the infinite spectral series, linearizes the equations, and applies a numerical finite difference scheme. The key steps in this solution are discussed next.

As a first step, write p_n as its real and imaginary parts,

$$p_n = h_n - jg_n \quad (20)$$

where

$$h_n = \frac{1}{\pi} \int_{-\pi}^{\pi} p(\tau) \cos(n\tau) d\tau \quad (21)$$

and

$$g_n = \frac{1}{\pi} \int_{-\pi}^{\pi} p(\tau) \sin(n\tau) d\tau. \quad (22)$$

Substituting Eq. 22 into Eq. 19, and separating real and imaginary parts yields the infinite set of coupled partial differential equations for h_n and g_n given in Eq. 23 and 24.

$$\begin{aligned} \frac{\partial h_n}{\partial \sigma} + \frac{d}{4n z_0} \frac{\partial^2 g_n}{\partial r^2} + \alpha d n^2 h_n \\ = \frac{dn}{2l_d} \left[\sum_{k=1}^{n-1} (g_k h_{n-k} + h_k g_{n-k}) - 2 \sum_{k=n+1}^{\infty} (h_k g_{k-n} - g_k h_{k-n}) \right] \end{aligned} \quad (23)$$

$$\begin{aligned} \frac{\partial g_n}{\partial \sigma} - \frac{d}{4n z_0} \frac{\partial^2 h_n}{\partial r^2} + \alpha d n^2 g_n \\ = \frac{dn}{2l_d} \left[\sum_{k=1}^{n-1} (g_k g_{n-k} - h_k h_{n-k}) - 2 \sum_{k=n+1}^{\infty} (h_k h_{k-n} + g_k g_{k-n}) \right] \end{aligned} \quad (24)$$

Given an axi-symmetric source, with time history such as $\sin\tau$, the coupled differential equations describe the growth of harmonics due to nonlinearity and the modification of the sound field due to diffraction effects. Since the fundamental frequency corresponds to $n = 1$, the attenuation of these harmonics is determined by αn^2 which is equivalent to a square law attenuation term. The solutions can be adjusted to account for non-square law attenuation terms by replacing n^2 by n^g where g is the attenuation power law.

5.0 KZK Equation Numerical Solution

As discussed earlier, since no closed form solution exists for the KZK equation the usual approach is a numerical solution. The general approach consists of transforming Eqs. 23 and 24 into a series of linearized difference equations which can be solved using standard

numerical techniques⁶. Since the specific numerical solution is discussed in detail in a number of references, this section first focuses on the unique enhancements in computational efficiency that are implemented in current work - the dynamic allocation of harmonic terms in during the computation and the use of a floating boundary condition which increases computational throughput while avoiding some of the artificial boundary problems discussed at the 12th ISNA⁷ and second discusses the convergence of the numerical solution.

5.1 "Floating" or Expanding Boundary Condition

A traditional problem in finite difference calculations is the initial selection of the outer mesh size for the calculation. This is important since the pressure front expands radially as the sound propagates. The improper selection of the outer boundary of the calculational mesh can result in one of two of the possible outcomes:

- The creation of an artificial rigid boundary which creates an spurious reflections as the signal propagates. These reflections in turn "poison" the answer.
- An excessively slow calculation due to a large mesh size. The calculation rate is inversely proportional to the number of transverse mesh points in the finite difference calculation.

A simplistic approach can be used to prevent the inclusion of an artificial boundary and at improve computational efficiency. This approach is shown symbolically in Figure 3. When the pressure fundamental frequency spectral amplitude magnitude at the third point before the edge of the boundary, $A[n-3]$, exceeds a pre-specified threshold value two additional computational cells are added to the calculation. The expanding pressure front does not reach the rigid edge of the boundary. By expanding the boundary when required the calculation time can be reduced by as much as a factor of two, depending on the problem.

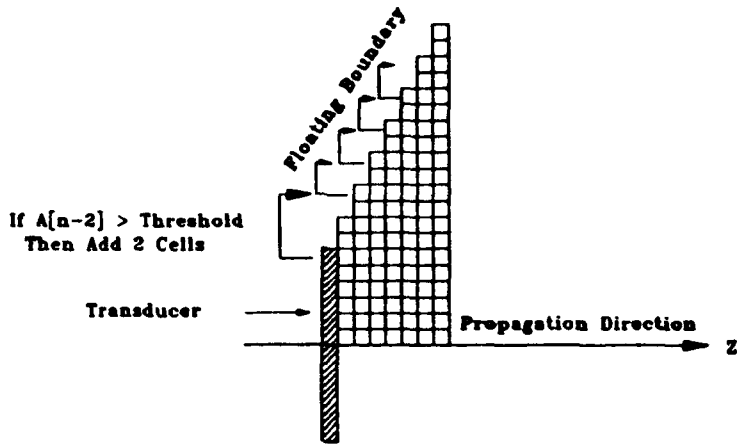


Figure 3. "Floating" boundary condition numerical technique

An example of the effectiveness of this technique is shown in Figure 4. In this instance, a line focused transducer with a 30° aperture angle is located at $z = 0$. The boundary at the start of the calculations was initially set to be 10% larger than the transducer physical boundary and the calculational threshold was varied between 1.0×10^{-4} and 1.0×10^{-12} . For the lowest threshold value the computational boundary expands by about a factor of 10 when propagating from the face of the transducer to 40% beyond the geometric focus. As the threshold for expanding the boundary is reduced the boundary expands at a faster rate, e.g. for a threshold of 1.0×10^{-12} the boundary has expanded an order of magnitude at a normalized distance 70% beyond the face of the transducer. Allowing the boundary condition to "float" increases the computational efficiency by a factor of two. A relatively simple and effective technique for improving computational efficiency.

A natural question is "how much error is introduced by this approximation?" This can be addressed by examining the normalized pressure amplitude for the propagating sound field over the range from $z = 0.4$ to 1.4 at a transverse location lined up with the edge of the transducer, e.g. 1.0 in Figure 4. These results are shown in Table 1 for four threshold values - 1.0×10^{-4} , 1.0×10^{-6} , 1.0×10^{-8} , and 1.0×10^{-10} . Once the threshold is decreased to $\sim 1.0 \times 10^{-6}$ there is essentially no difference in the numerical result.

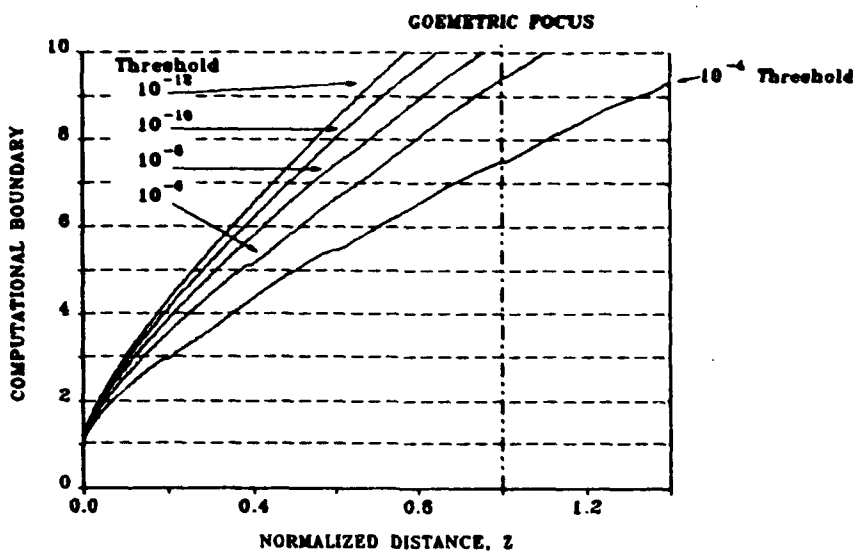


Figure 4. "Floating" boundary condition expansion

Table 1 - Boundary Threshold Impact On Precision

Z	THRESHOLD			
	10^{-18}	10^{-16}	10^{-14}	10^{-12}
0.4	0.038769598	0.038769408	0.038769408	0.038769408
0.5	0.027677476	0.027674593	0.027674592	0.027674592
0.6	0.038084044	0.038083162	0.038083161	0.038083161
0.7	0.043991060	0.043995829	0.043995831	0.043995831
0.8	0.011198938	0.011194064	0.011194065	0.011194065
0.9	0.039476849	0.039474818	0.039474820	0.039474820
1.0	0.063521380	0.063523095	0.063523093	0.063523093
1.1	0.057549026	0.057547647	0.057547643	0.057547643
1.2	0.030258185	0.030259337	0.030259324	0.030259324
1.3	0.073250350	0.073248796	0.073248786	0.073248786
1.4	0.110690431	0.110684937	0.110684927	0.110684927

5.2 Dynamic Allocation Of Harmonic Terms

The classic problem encountered in the numerical solution of nonlinear equations using a Fourier representation is the large number of harmonic terms that are required due to harmonic growth. If too few terms are used in the Fourier series which represents the solution, a truncation error occurs in last few terms which start to grow in magnitude abnormally. As this truncation error continues to increase it begins to affect the preceding terms. Eventually, the truncation error distorts the solution. Generally, to avoid this problem a number of alternatives are available, such as:

- increase the number of harmonics to push the truncation error further out,
- size the number of harmonics to the precision required and increase the attenuation of higher harmonics to compensate, or
- use either of the preceding and filter the output by discarding a number of higher harmonic terms where the truncation error is obvious.

In using any of these approaches, a sufficient number of harmonics has to be retained to provide the basic precision required in the output. In general regardless of the approach used, the computational efficiency is proportional to the number of harmonics squared.

A simple computational solution is available consistent with the physics of the process. The basic algorithm is shown symbolically in Figure 3. At the beginning of the computation a minimum number of harmonics are allowed in the computation. All harmonic terms are initialized to zero. At each longitudinal step in the computation, the magnitude of the last harmonic is checked, if it is above a preset threshold another harmonic term is added.

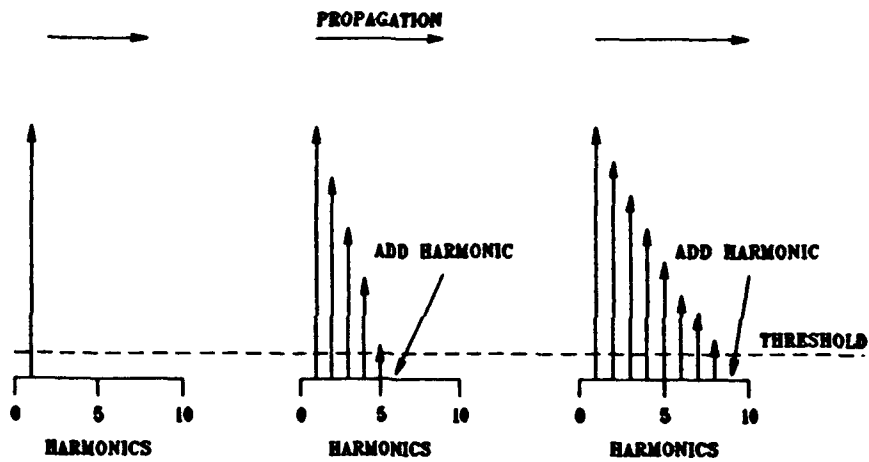


Figure 3. Dynamic harmonic allocation process.

The threshold is selected as a fraction of the normalized peak initial pressure amplitude. The impact of different threshold choices is shown in Tables 2, 3, and 4. At the beginning of the calculation the maximum number of harmonic terms is set to four. Table 3 is the on-axis amplitude spectra at $z = 0.4$ when the threshold is varied from 1.0×10^{-4} to 1.0×10^{-12} . The amplitude spectra magnitude displayed to four significant figures. N is the number of the spectral term with 1 corresponding to the fundamental frequency, 2 the first harmonic, etc.. Powers of ten in the table are designated by $E \pm xx$ which represents $10^{\pm xx}$.

In Table 2 changing the threshold over the range 1.0×10^{-4} to 1.0×10^{-12} has virtually no impact on the magnitude of the fundamental and the first three harmonics, at least to four significant figures. The additional harmonic terms generated when the threshold is set to 1.0×10^{-8} or less appear to have no impact on the magnitude of the fundamental and the first three harmonics. However, at this point the pulse has only propagated 40% of the distance to the geometric focal point and very little harmonic generation has taken place. A better perspective can be obtained by examining the spectra at $z = 0.9$ which is just before the geometric focus. This comparison is shown in Table 3 below. Again, to five

significant figures, the magnitude of the fundamental and the first four harmonics appears is unaffected by threshold values below 1.0×10^{-8} .

Table 2. On-axis spectra at $z = 0.4$

THRESHOLD					
n	10^{-4}	10^{-6}	10^{-8}	10^{-10}	10^{-12}
1	1.0935E+00	1.0935E+00	1.0935E+00	1.0935E+00	1.0935E+00
2	4.7449E-03	4.7449E-03	4.7449E-03	4.7449E-03	4.7449E-03
3	2.8661E-05	2.8661E-05	2.8661E-05	2.8661E-05	2.0568E-07
4	2.0568E-07	2.0568E-07	2.0567E-07	2.0567E-07	2.0568E-07
5			1.5917E-09	1.6205E-09	1.6207E-09
6				1.3132E-11	1.3559E-11
7					1.1274E-13

Table 3. On-axis spectra at $z = 0.9$

THRESHOLD					
n	10^{-4}	10^{-6}	10^{-8}	10^{-10}	10^{-12}
1	1.7435E+00	1.7435E+00	1.7435E+00	1.7435E+00	1.7435E+00
2	1.9786E-02	1.9786E-02	1.9786E-02	1.9786E-02	1.9786E-02
3	3.2627E-04	3.2627E-04	3.2627E-04	3.2627E-04	3.2627E-04
4	6.3104E-06	6.3097E-06	6.3093E-06	6.3093E-06	6.3093E-06
5		1.1583E-07	1.3336E-07	1.3339E-07	1.3339E-07
6			2.8353E-09	2.9856E-09	2.9860E-09
7				6.8332E-11	6.9557E-11
8					1.6588E-12
9					1.8266E-14

A last check on the impact of the threshold magnitude is shown in Table 4 which lists the on-axis amplitude spectra 40% beyond the geometric focus ($z = 1.4$). Again, for a threshold between 1.0×10^{-6} and 1.0×10^{-3} there is no significant impact on harmonic magnitude.

Table 4. On-axis spectra at $z = 1.4$

n	THRESHOLD				
	10^{-4}	10^{-6}	10^{-8}	10^{-10}	10^{-12}
1	1.2942E+00	1.2942E+00	1.2942E+00	1.2942E+00	1.2942E+00
2	2.1359E-02	2.1359E-02	2.1359E-02	2.1359E-02	2.1359E-02
3	5.3937E-04	5.3937E-04	5.3937E-04	5.3937E-04	5.3937E-04
4	1.6275E-05	1.6269E-05	1.6269E-05	1.6269E-05	1.6269E-05
5		5.4167E-07	5.4018E-07	5.4017E-07	5.4017E-07
6			1.9115E-08	1.9043E-08	1.9043E-08
7			5.7185E-10	7.0054E-10	6.9950E-10
8				2.7133E-11	2.6488E-11
9					1.0397E-12
10					2.8673E-15

5.3 Numerical Solution Convergence

To assure that the numerical solution converges the transverse and longitudinal step size are reduced until the change in the numerical solution is insignificant. Figure 4 shows the on-axis normalized peak pressure amplitude as a function of the radial step size used in finite difference solution of the KZK equation.

In this calculation the phase of the initial pressure is corrected using a quasi-optical approximation. As dr decreases from a normalized value of 2% of the transverse radius ($dr = 0.02$) to 1% ($dr = 0.01$) the peak pressure profile changes dramatically. However, as the mesh size decreases the solution essentially converges, at least to a visual inspection. The rate of convergence is shown in Table 5 which contains the value of dr , and the magnitude of the on-axis pressure fundamental, 2nd, and 3rd harmonics. As dr decreases the harmonics converge to their asymptotic values. By the time that $dr = 0.004$ the location of the predicted focal point has changed and the magnitude of each harmonic has converged to a point that the jitter is on the order of a few parts per thousand.

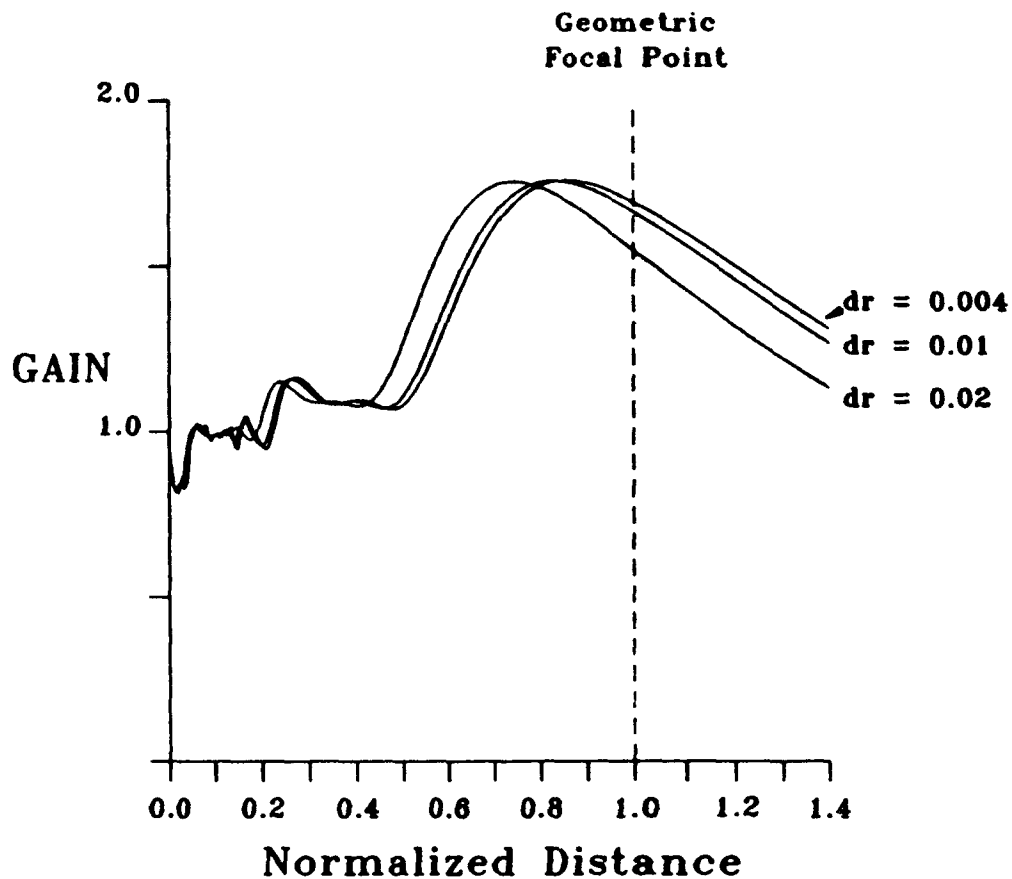


Figure 4. On-axis normalized peak pressure convergence

Table 5. Solution convergence at predicted focal point.

dr	z	$A_n(1)$	$A_n(2)$	$A_n(3)$
0.0200	7.4247E-0001	1.7489E+0000	1.8391E-0002	2.8168E-0004
0.0100	8.2500E-0001	1.7519E+0000	1.8301E-0002	2.7682E-0004
0.0075	8.5439E-0001	1.7532E+0000	1.8421E-0002	2.8030E-0004
0.0050	8.5000E-0001	1.7528E+0000	1.8312E-0002	2.7693E-0004
0.0040	8.5439E-0001	1.7529E+0000	1.8354E-0002	2.7822E-0004
0.0030	8.5439E-0001	1.7532E+0000	1.8368E-0002	2.7860E-0004

To obtain a better approximation for the pressure in the focal region an amplitude shading can be applied as discussed in Section 4. The calculated on axis peak pressure using both phase and amplitude shading is compared in Figure 5 to the calculated peak pressure using only phase shading. The difference for the 30° aperture is only a few percent in peak amplitude at the focal point and the location of the calculated focal point does not change as a result of amplitude shading.

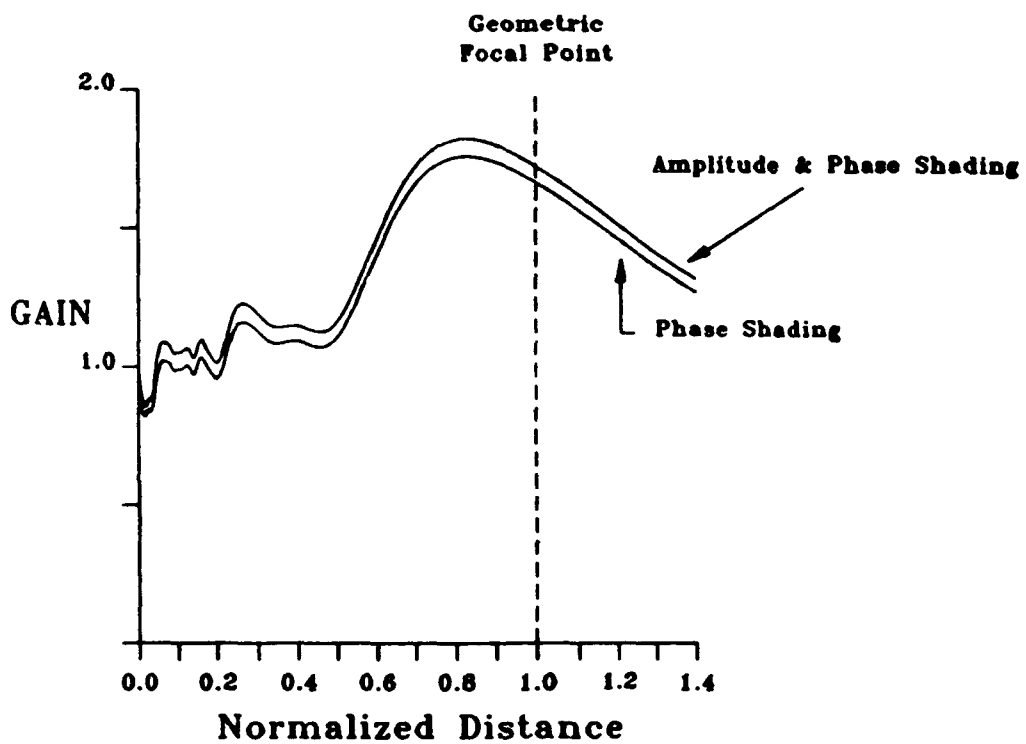


Figure 5. Amplitude and phase shading comparison

6.0 KZK Line focus equation numerical predictions

This section presents the predicted pressure profile for the experimental configuration. The inputs for the solution are summarized in section 6.1. The predicted peak pressure profile on and off the symmetry axis are shown in Section 6.2. The change in the pressure time history due to non-linear effects is shown in Section 6.3 when the peak initial pressure across the aperture is changed by an order of magnitude.

6.1 Initial conditions

The normalized initial peak pressure profile at the face of the transducer is shown in Figure 6. The line focus transducer enclosed aperture is approximately 30° .

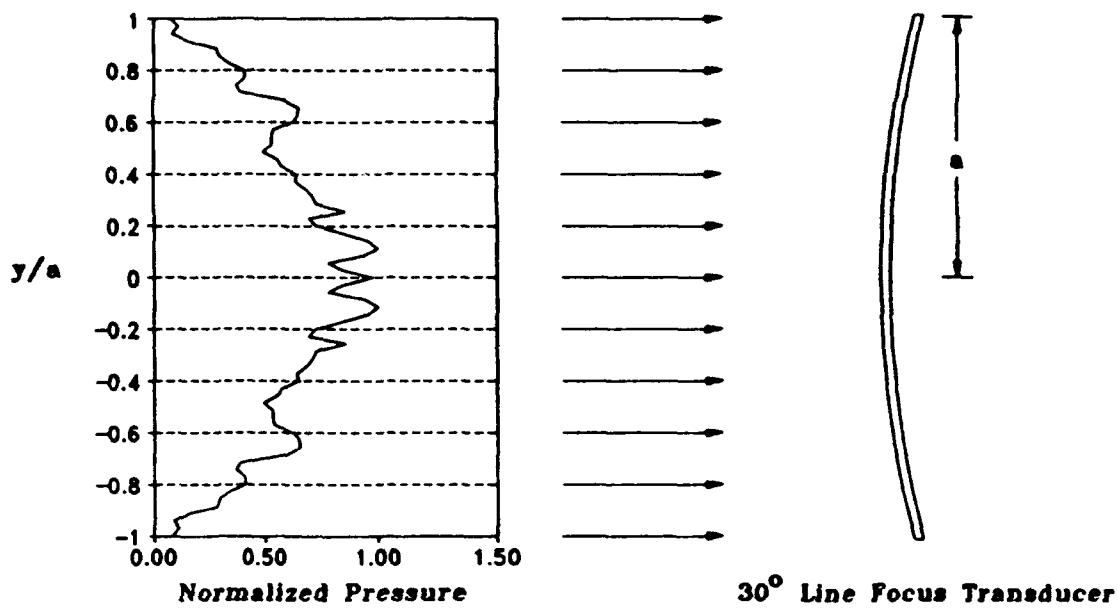


Figure 6. Initial pressure profile at transducer face.

The peak pressure at the face of the transducer is approximately 58.05 kPa. The transducer radius of curvature is 0.04445 m with a transverse radius of 0.01151 m. The input driving frequency is 1.0667 MHz. The transducer is in water with: density, 9.98 Kg/m³; velocity, 1492 m/s; and B/A, 5.5. The calculations were performed with the thresholding for the floating boundary and the dynamic harmonic allocation set to 10^4 . The transverse step size was set to 4.0×10^{-3} .

6.2 Peak Pressure Profile - 58.05 kPa source

A three dimensional plot of the pressure profile is shown in Figure 7. The vertical (y) axis is the peak pressure normalized to the initial peak pressure at the face of the transducer.

The horizontal (x) axis is the range from the transducer symmetry axis. The z axis is the normalized distance along the direction of propagation.

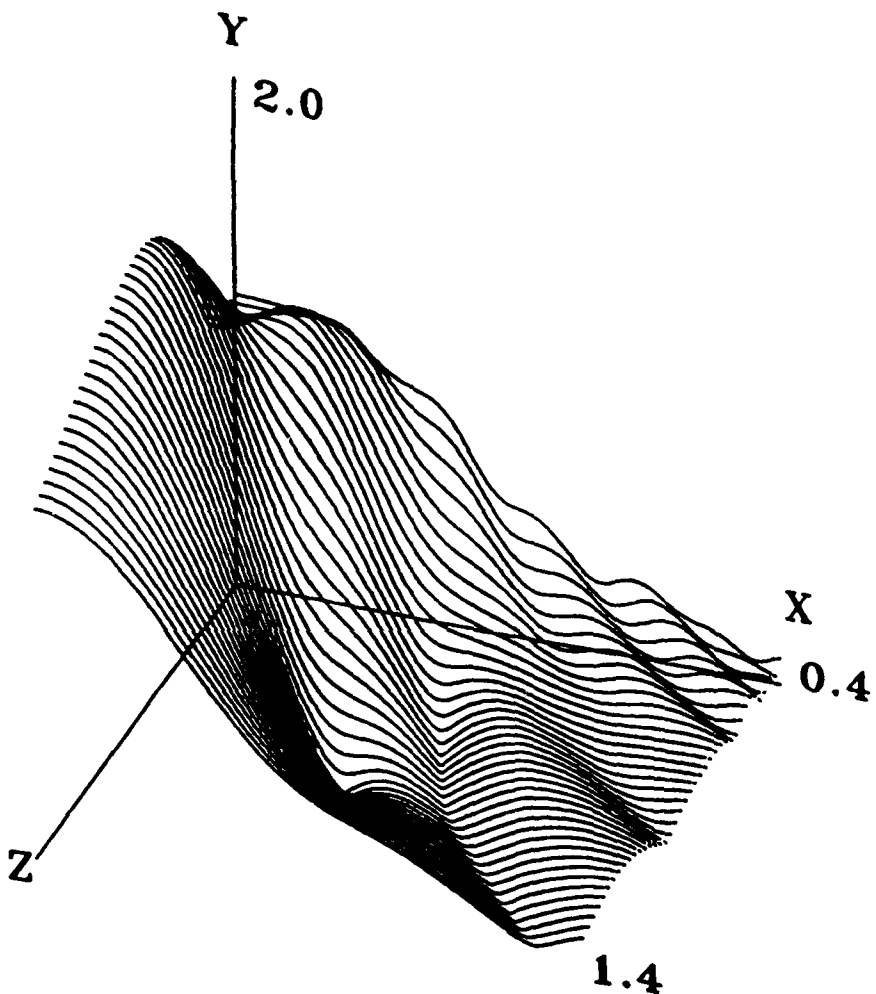


Figure 7. Peak pressure profile transverse to the propagation direction.

Individual peak pressure profile segments are shown in Figure 8 for as the normalized distance increased from $z = 0.4$ to $z = 1.3$. This shows the growth in the on-axis pressure as the geometric focus is approached and the subsequent decrease in intensity after the geometric focus.

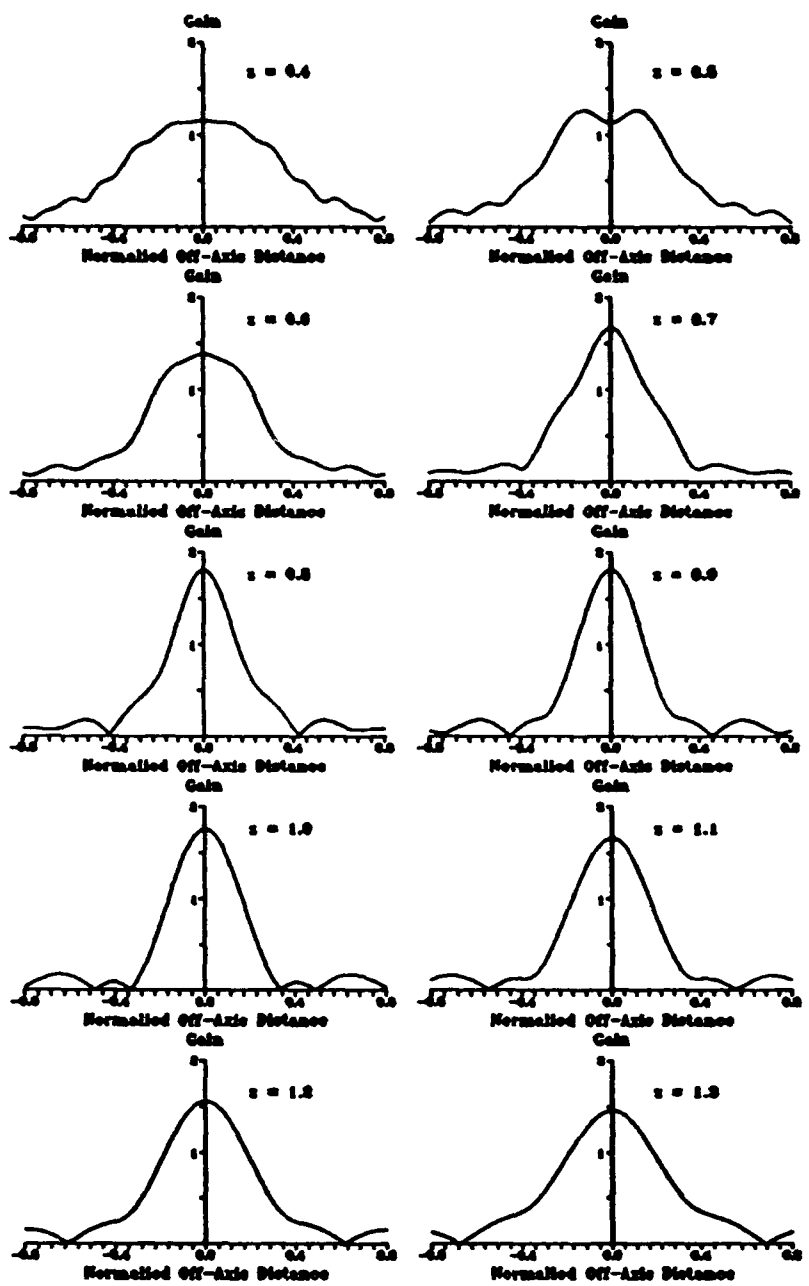


Figure 8. Transverse peak pressure profile vs normalized distance.

Since the peak pressure is predicted to occur at $z \approx 0.86$, Figure 9 illustrates the growth in peak pressure through the region $z = 0.8$ through $z = 0.92$.

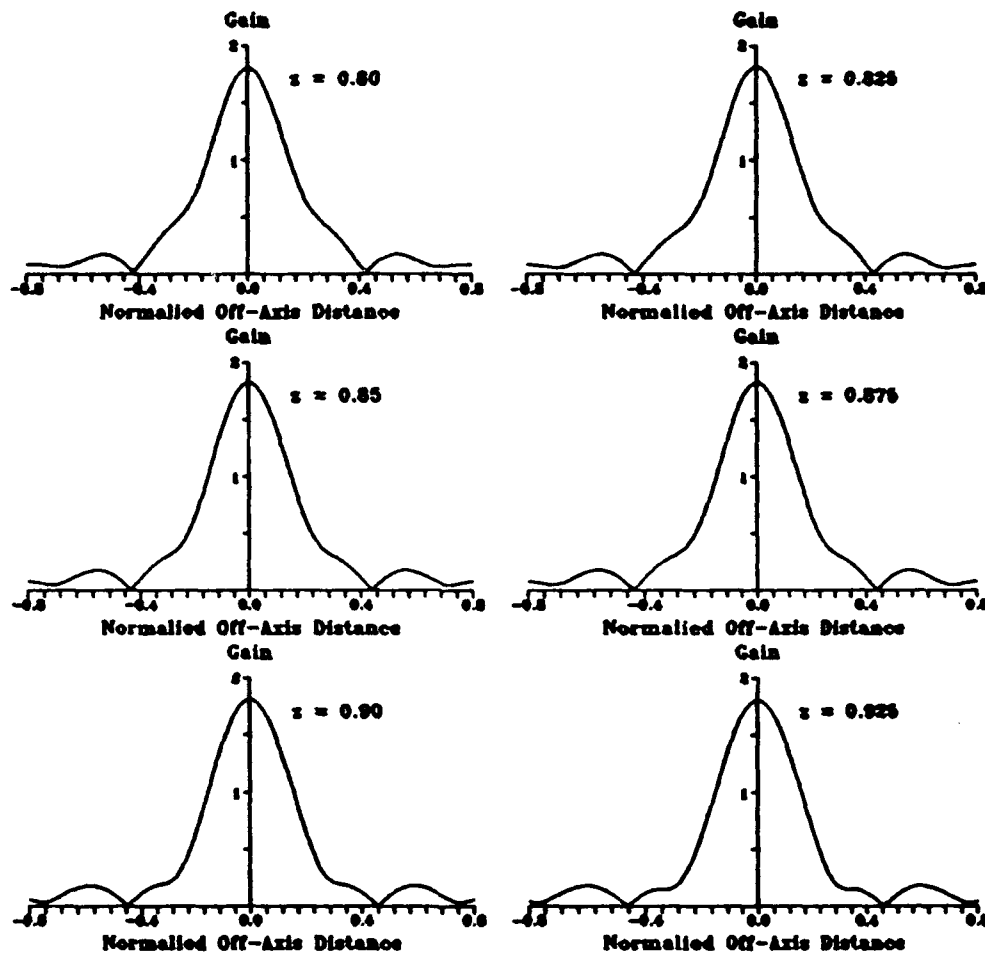


Figure 9. Transverse pressure profile around focal point.

6.3 Predicted Impact of Increased Pressure

When the initial pressure is increased the growth in higher harmonics is accelerated. The change in the pressure time history for initial pressures of 58.05 kPa and 508.5 kPa is shown in Figure 10. The time domain wave shape is becoming asymmetric which is

characteristic of the growth in higher harmonics, e.g. 5 significant harmonics at 58.05 kPa and 10 significant harmonics at 580.05 kPa. At the same time there is a slight shift in the location of the predicted focal, as shown in Figure 11.

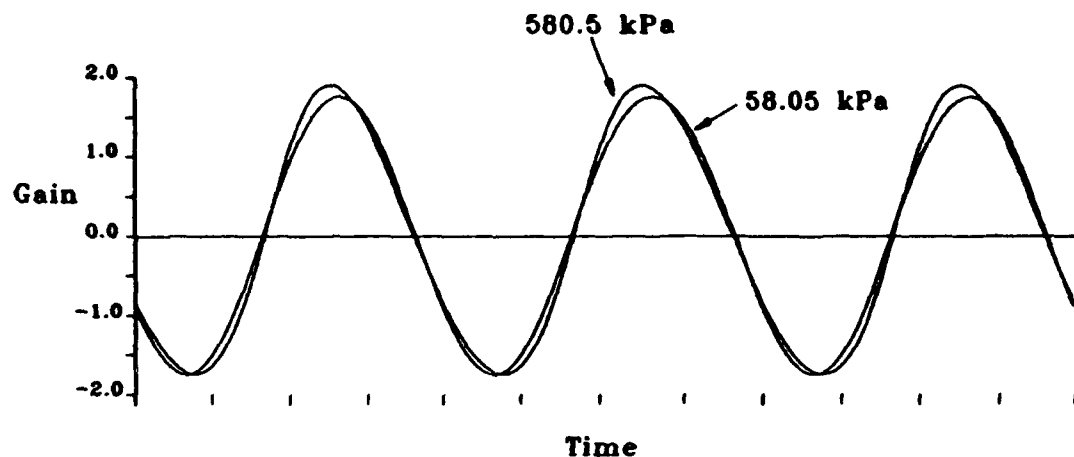


Figure 10. Distortion in time-domain waveform due to harmonic growth.

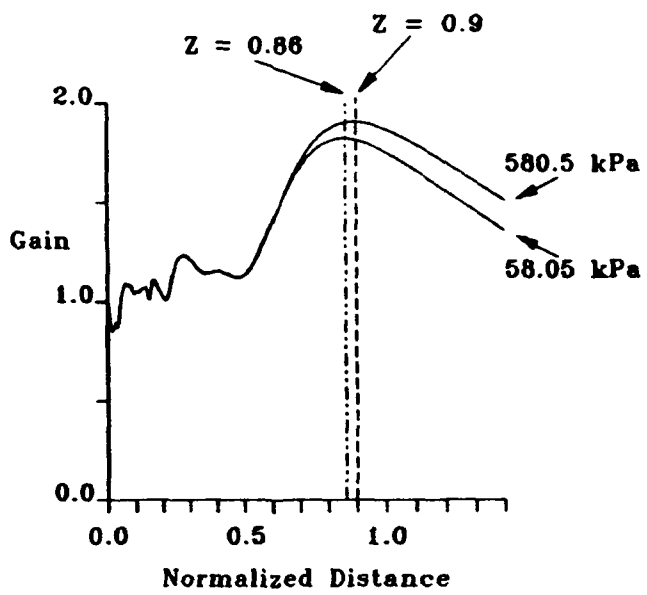


Figure 11. Shift in predicted focal point due to increased pressure.

References

1. N. S. Bakhvalov, Ya. M. Zhileikin, and E. A. Zabolotskaya, Nonlinear Theory of Sound Beams, American Institute of Physics, New York (1987).
2. J. Naze Tjøtta and S. Tjøtta, "Nonlinear equations of acoustics, with application to parametric acoustic arrays," J. Acoust. Soc. Am. 69, 1644-1652 [1981].
3. B. K. Novikov, O. V. Rudenko, and V. I. Timoshenko, Nonlinear Underwater Acoustics, Acoustical Society of America, New York (1987).
4. S. I. Aanonsen, "Numerical computation of the nearfield of a finite amplitude sound beam," Rep. No. 73, Department of Mathematics, University of Bergen, Bergen Norway (1983).
5. T. S. Hart and M. F. Hamilton, "Nonlinear effects in focused sound beams," etc.
6. W. F. Ames, Numerical Methods for Partial Differential Equations, Academic Press, New York (1977).
7. M. F. Hamilton and D. T. Blackstock, Frontiers of Nonlinear Acoustics, 12th ISNA, Elsevier Applied Science, London (1990).

Summary Page II

This section contains a condensed version of the theory developed in the previous section; it was presented by Dr. Neighbors at the 1993 International Symposium on Nonlinear Acoustics in Norway.

Also contained in this section is a condensed version of a paper presented by Dr. Ruf at the 1993 Ultrasonics International Conference in Austria. It details the interpretation of the pressure distribution within a focused sound field by making use of the acousto-optic Schlieren image produced by this field and the use of a CCD detector to map this field. The Schlieren image evaluation and the conventional pinducer field mapping techniques were compared and the field distortion due to the presence of the pinducer probe were noted.

FOCUSED ULTRASOUND IMAGING

Thomas H. Neighbors, Herbert J. Ruf, and Walter G. Mayer
Ultrasonics Research Laboratory, Physics Department
Georgetown University, Washington, D.C. 20057-0995 USA

ABSTRACT

Today, focused sound field measurements typically involve needle or membrane type transducers stepped across the sound field. This time consuming process is limited by probe linearity, effective aperture size, and experimental alignment. In the past, Schlieren imaging has provided an effective, qualitative technique for examining a sound pressure field. This paper extends the Schlieren technique to provide quantitative measurements of the entire focused sound pressure field without in-situ disruptions. Theoretical sound pressure field predictions for a line focused system are made based on a numerical solution of the Khokhlov-Zabolotskaya-Kuznetsov parabolic equation. Enhancements in computational effectiveness of the numerical solution are discussed and key features of the experimental setup outlined. The theoretical predictions are compared with experimental measurements made with the extended Schlieren technique.

1. Introduction

Since Raman-Nath¹ theory was published 60 years ago, acousto-optic techniques have been used for non-interactively measuring sound pressure fields. The diverse applications have ranged from the examination of harmonic growth² to sound pressure field reconstruction using tomography techniques. Schlieren imaging as developed by Hiedemann³ et al has been used extensively to image the entire sound field through photographic images.

The propagating sound pressure for a line focused radiator is predicted using the Khokhlov-Zabolotskaya-Kuznetsov (KZK) parabolic equation. Enhancements in the numerical solution are outlined and the experimental setup for the enhanced Schlieren technique summarized. Predicted and measured on- and off-axis pressure profiles are then compared.

2 Line Focused KZK Equation

The KZK parabolic equation, Eq. (1), is used to describe the propagation of a directive finite amplitude sound beam including nonlinearity, diffraction and attenuation⁴. P is the sound pressure; z is the on-axis distance; t' is the

retarded time ($t - z/c_0$), with c_0 the isentropic speed of sound; ∇_\perp^2 is the transverse Laplacian; ρ_0 is the fluid density; and β is the coefficient of nonlinearity.

$$\frac{\partial^2 P}{\partial z \partial t'} - \frac{c_0}{2} \nabla_\perp^2 P - \frac{b}{2\rho_0 c_0^3} \frac{\partial^3 P}{\partial t'^3} = \frac{\beta}{2\rho_0 c_0^3} \frac{\partial^2 P^2}{\partial t'^2} \quad (1)$$

The $\nabla_\perp^2 P$ term corresponds to diffraction effects. In Eq. (1) a well collimated beam is assumed, e.g. $ka \gg 1$ with $k = \omega/c_0$ and a = the source radius.

For a line source, which considers only the yz plane and ignores yx plane variations, the transverse Laplacian can be replaced with $\partial^2 y$. Eq. (2) is the line source KZK equation. It has been simplified by replacing the retarded time by a normalized retarded time, i.e. $\tau = wt'$; the pressure P by a normalized pressure $p = P/p_0$, where p_0 is the initial on-axis peak pressure; manipulating a few terms; and using standard definitions of the Rayleigh distance, z_0 , discontinuity distance, l_d , and the thermal viscous loss coefficient α ,

$$\frac{\partial^2 p}{\partial \sigma \partial \tau} - \frac{d}{4z_0} \frac{\partial^2 p}{\partial \tau^2} - \alpha d \frac{\partial^3 p}{\partial \tau^3} = \frac{d}{2l_d} \frac{\partial^2 p^2}{\partial \tau^2} \quad (2)$$

If p is expanded as a Fourier series as indicated in Eq. (3) where p_n is the complex Fourier coefficient, Eq. (2) becomes the series of coupled partial differential equations for the Fourier amplitude coefficients, shown in Eq. (4).

$$p = \sum_{n=-\infty}^{\infty} p_n e^{j n \tau} \quad (3)$$

$$jn \frac{\partial p_n}{\partial \sigma} - \frac{d}{4z_0} \frac{\partial^2 p_n}{\partial \tau^2} - \alpha d(jn)^3 p_n = \frac{d(jn)^2}{2l_d} \left[\sum_{k=1}^{n-1} p_k p_{n-k} + 2 \sum_{k=n+1}^{\infty} p_k p_{k-n} \right] \quad (4)$$

Since the fundamental frequency corresponds to $n = 1$, harmonic attenuation is determined by αn^2 . To account for non-square-law attenuation replace n^2 by n^g where g is the attenuation rate.

Since a general analytic solution of the KZK equation has not been found to date, Eq. (4) is usually solved by numerical techniques. The approach used here has been adapted from the numerical solution initially developed by Aanonsen⁵, enhanced by Hart and Hamilton⁶, and revised by Neighbors and Bjørne⁷. Computational efficiency is enhanced by floating the transverse

boundary condition and dynamically allocating harmonic terms.

A traditional problem in finite difference calculations is the calculation's outer mesh size. The simple approach shown in Figure 1 prevents the inclusion of an artificial boundary and improves computational efficiency. When the pressure fundamental frequency magnitude at the third point before the edge of the boundary, $A[n-2]$, exceeds a pre-specified threshold value, additional cells are added. This causes the boundary to move as the pressure increases near the boundary. This approach prevents artificial reflections at the numerical boundary and the calculation time is reduced by up to a factor of two, depending on the problem.

The second problem encountered in the numerical solution of nonlinear equations is the large number of harmonic terms required due to harmonic

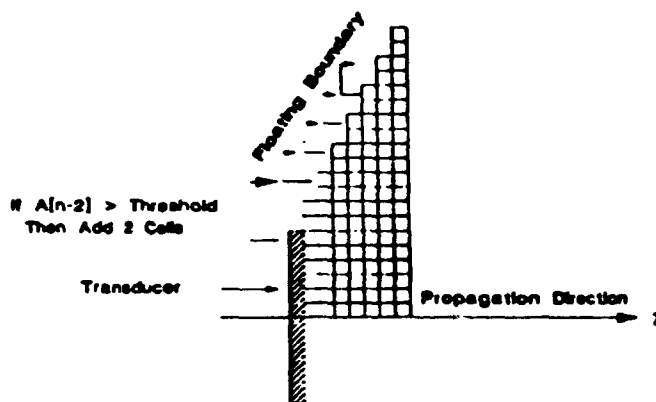


Figure 1. "Floating" transverse boundary condition.

growth. In general, computational efficiency is proportional to the number of harmonics squared. A simple solution is available consistent with the physics of the process. At the beginning of the computation, a minimum number of harmonics are included. At each longitudinal step in the calculation, the last harmonic's magnitude is checked. If it is above a preset threshold, another harmonic is added. This improves the computational efficiency by several factors without any loss in numerical precision or stability.

3. Enhanced Schlieren Imaging

Figure 2 illustrates the experimental setup⁸. Light from a 20 mW, He-Ne Laser is incident on a short focal length lens which has its focal point at

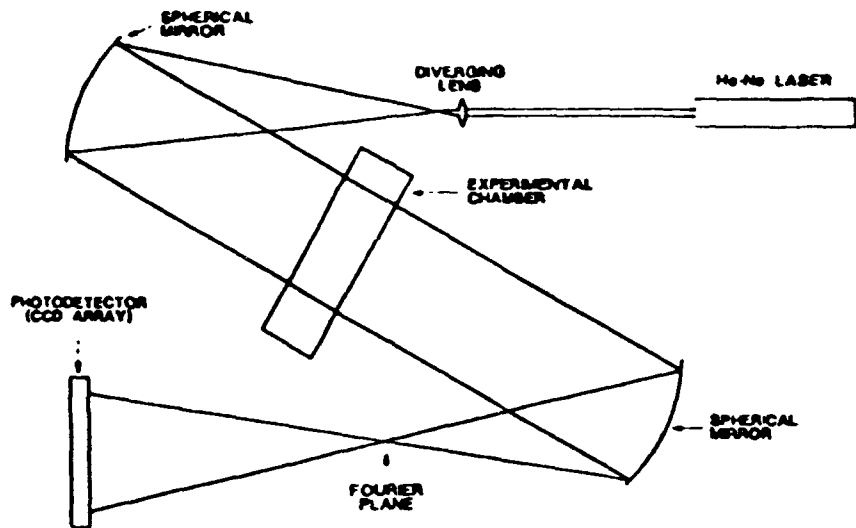


Figure 2. Z-configuration Schlieren image system

the spherical mirror's focal point (4 m). Thus the reflection from the mirror is collimated. When the beam passes through a water tank containing the line focus transducer, it is diffracted by the focused sound field. The light is focused by the second spherical mirror into a diffraction pattern on the Fourier plane. By blocking all but the positive and negative first diffraction orders at the Fourier plane, the sound field image contained is incident on the Charge Coupled Device (CCD) array at the image plane. The magnitude of the pressure to first order is given by the light intensity, $I_1 = J_1^2(v)$ where $v = 2\pi\mu L/\lambda$ is the Raman-Nath parameter with μ the maximum variation in the index of refraction caused by the pressure, L the width of the sound beam, and λ the light wavelength. The CCD detector used in the experiment is a Fairchild Weston Systems model CCD181, which has 2592 active elements in a linear array with a dynamic range of 7500:1 relative to rms noise. The line focused transducers were constructed by Channel Industries of PZT-4 with a thickness of 0.625 cm and a radius of curvature of 4.445 cm. During the series of experiments conducted three aperture angles of 30°, 60°, and 90° were used.

4. Comparison Between Theory And Experiment

The peak pressure profile at the face of the 30° aperture transducer is shown in Figure 3 normalized to the on-axis pressure at the transducer face which was 77.31 kPa. The transducer radius of curvature is 4.445 cm with a transverse radius of 1.151 cm. The input driving frequency is 1.1 MHz and the tank was filled with water. The numerical values of the density, isentropic

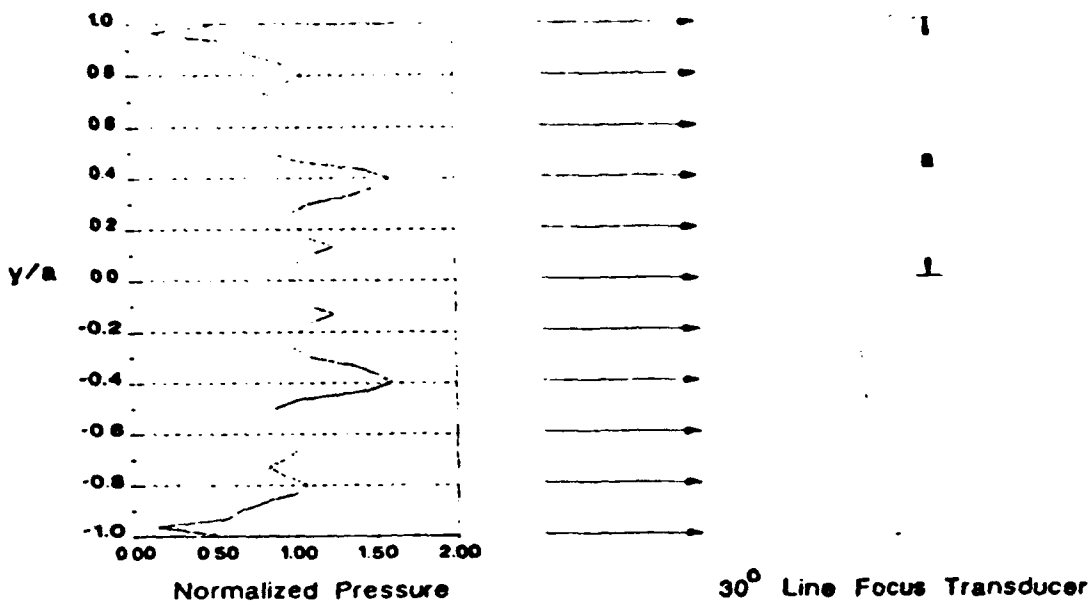


Figure 3. Initial pressure profile at transducer face.

velocity, and B/A of water were taken as 9.98 kg/m^3 , 1492 m/s , and 5.5 , respectively.

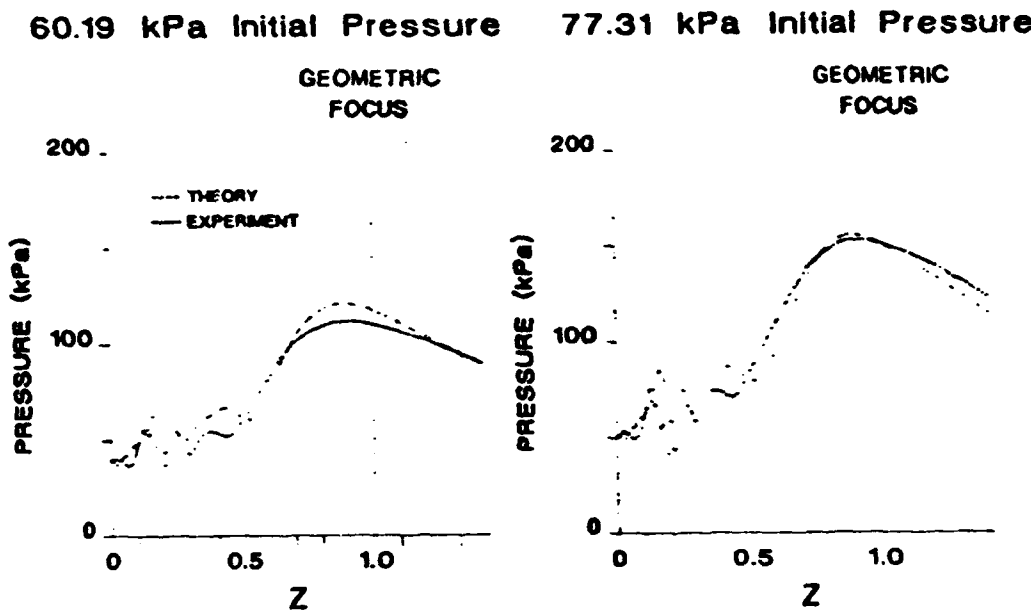


Figure 4. On-axis peak pressure experimental vs predicted profiles.

To predict the on- and off-axis pressure using the line source KZK approximation, the amplitude and phase at the transducer face were adjusted using a quasi-optical approximation. The calculations were performed with the threshold for the floating boundary and harmonic allocation set to 10^{-6} and a transverse step size of 4.0×10^{-3} . Figure 4 is a comparison of the predicted and measured on-axis sound pressure for a 60.19 kPa and 77.31 kPa sources. The dashed line is the theoretical prediction using the line focus KZK equation. The solid line is the experimental result measured using the extended Schlieren technique. The difference between the predicted and measured focal point is approximately 4% and the variation in peak pressure is between 10% (60.19 kPa source) and 1% (77.31 kPa source). In both cases the quantitative agreement between theory and experiment is relatively good.

5. Acknowledgements

This work was supported by the U.S. Office of Naval Research and by the Scientific Affairs Division, NATO.

6. References

1. C. V. Raman, *Proc. Ind. Acad. Sci. II* (1935) 406.
2. W. G. Mayer and T. H. Neighbors, *Ultrasonics* 25 (1987) 83.
3. E. Hiedemann, *Ultraschallforschung*. (Walter De Gruyer & Co, Berlin, 1939).
4. N. S. Bakhvalov, Ya. M. Zhileikin, and E. A. Zabolotskaya, *Nonlinear Theory of Sound Beams*, (AIP, New York, 1987).
5. S. I. Aanonsen, *Numerical computation of the nearfield of a finite amplitude sound beam*, (Rep. No. 73, Department of Mathematics, University of Bergen, Bergen, 1983).
6. T. S. Hart and M. F. Hamilton, *JASA* 84 (1988) 1488.
7. T. H. Neighbors and L. Bjørne, *A study of the KZK equation*, (Rep. No. 13, LIA, Technical University of Denmark, Lyngby, 1988).
8. H. J. Ruf, *An acousto-optic investigation of focused ultrasonic fields*, (Dissertation, Georgetown University, Washington, 1991).

Acousto-Optic Measurement of Pressure Profiles in Ultrasonic Fields

Herbert J. Ruf

Physics Department, Georgetown University, Washington, DC 20057

A Charge-Coupled Device (CCD) detector is used in a Schlieren imaging system to determine pressure profiles in an ultrasonic field. The ultrasonic field studied is from a 1.10 MHz line focus transducer in water, operated in the Raman-Nath regime. The Schlieren images are made using only the first diffraction orders. Comparison of pressure profiles made with a conventional PVDF needle hydrophone are used to demonstrate the usefulness of the Schlieren imaging technique.

INTRODUCTION

Schlieren imaging has been used for decades to produce photographs of ultrasonic fields and to investigate ultrasonic propagation through studies of the diffraction patterns produced. Schlieren systems have been utilized by Haran [1] to measure the total acoustic power in an ultrasonic beam and by Reibold [2] to determine the pressure distribution in an ultrasonic field. The work reported here demonstrates a method by which the axial pressure profile of a line focus transducer can be measured. Advantages of this method lie in the spatial resolution of the optical detector and in the fact that no mechanical scanning is necessary.

THEORETICAL CONSIDERATIONS

In a Schlieren imaging system a collimated beam of light passes through a region of varying refractive index. The portion of the light which is scattered by the variation in refractive index forms an image of the index variations. In this paper the index variations are caused by the pressure gradient induced in water by an ultrasonic field. The interaction of a progressive, sinusoidal ultrasonic wave with a light beam of normal incidence was first discussed by Raman and Nath [3]. The pressure gradient behaves as a phase grating which produces a diffraction pattern where the intensity of light in the n th order is given by

$$I_{\pm n} = J_n^2(v). \quad (1)$$

J_n is the n th-order Bessel function and v is the Raman-Nath parameter, which is proportional to pressure. If only the light from the $\pm n$ th diffraction orders is allowed to pass a spatial filter to form an image, then the light

intensity at each point of the image is proportional to I_{11} , in eq. (1). Thus, in principle, given an image of an ultrasonic field, one can determine the pressure field from which this image arose.

Since v is proportional to the pressure produced by an ultrasonic transducer, and the pressure is proportional to the excitation voltage applied to the transducer, V , the image intensity is a function of V . By varying V , and recording the intensity of any point in the Schlieren image as a function of V , data will be acquired which will allow a determination of the v value at this point, and therefore the pressure.

EXPERIMENT

A Schlieren imaging system in a Z-configuration [4] consisting of a He-Ne laser, a spherical mirror of 4m focal length as the focusing element, and a spatial filter consisting of two rectangular slits which allows the ± 1 diffraction orders to pass, were used for this experiment. The optical detector used in the image plane was a 2592-element, Fairchild linear CCD array, with a 10 μm distance between pixel centers. The active area of the CCD array is 2.54 cm and the Schlieren system was constructed so as to allow a 8.2 cm region to be imaged by the CCD, resulting in a distance between pixels of 63 μm .

The ultrasonic sources were constructed with PZT-4A line focus crystals, with a radius of curvature of 4.445 cm and a nominal resonant frequency of 330 kHz, the transducers were operated at the third harmonic at a frequency of 1.08 MHz. Two transducers were used, the first with a 30° arc and the second with 60° arc. The Raman-Nath theory assumes a uniform acoustic field in the direction of light propagation. This is not possible with a circular aperture transducer, so line focus transducers were utilized giving a rectangular cross-section to the acoustic field. The focused beam allowed for accurate placement of the CCD array and of the needle hydrophones used for a conventional pressure measurement comparison. Data were acquired over a range of 10 to 250 mV excitation voltage, nominally amplified by 50 dB, in 5 mV steps, all acquisition was done by computer with a data acquisition time of 0.16 ms per voltage step, all data were acquired within 20 minutes. Voltage was applied for short durations at each step to limit heat generation by the transducers and to reduce ultrasonic streaming.

ANALYSIS

A typical Intensity vs. V curve is shown in Fig. 1. Note that the intensity values are the raw intensity values as measured from the CCD. Modeling these data values with the expression,

$$I = C_1 J_1^2(C_2 V + C_3), \quad (2)$$

one may utilize a curve fitting procedure to determine the constants C_1 , C_2 , and C_3 . From these data the argument of the Bessel function, v , can be calculated. Pressure can then be calculated from v using the relationship

$$P = (0.65v)/L, \quad (3)$$

where P is pressure, L is the acoustic beam width that the light traverses.

The constant 0.65 in eq. (3) comes from an expression derived by Willard [5] which depends on the frequencies of the light and the sound beam, as well as the refractive index of the medium, water in this case. The beam width was found by scanning the transducer along the direction of light propagation with a needle hydrophone. The product of the ratio of the average to peak pressure, with the transducer crystal width, yields L. These beam scans are shown in Figs. 2 and 3 and demonstrate that there is no more than 2° of beam spread.

RESULTS AND CONCLUSIONS

Figures 4 and 5 compare the pressure profiles generated by the above procedure with profiles generated using a needle hydrophone in a scanning tank. Discrepancies between the optical and conventional profiles can be attributed to two causes, 1) there is a certain amount of uncertainty in the conventional scans due to possible uncertainty in the calibration of the hydrophones, and 2) Fig. 6 shows the effect of the presence of the hydrophone on the acoustic field, resulting in elevated pressure values. There is also a periodic structure visible in the conventional data, in particular for the 30° transducer, which is caused by standing waves between the transducer and the hydrophone.

Pressure profiles of line focus transducers were obtained using a noninvasive optical technique and compared with pressure profiles obtained with conventional hydrophone measurements. A pressure artifact, on the order of 5%, caused by the presence of the conventional hydrophone was demonstrated for measurements made in the focal region. Otherwise overall agreement between the two methods was found to be good.

ACKNOWLEDGEMENTS

This work was supported by the Office of Naval Research, U.S. Navy. The authors wish to thank, Dr. Leif Bjørnø for the loan of the needle hydrophones and the FDA-CDRH Laboratory for the use of their scanning tanks.

REFERENCES

- 1 M. Haran, B. D. Cook, and H. F. Stewart, Comparison of an Acousto-optic and a Radiation Force Method of Measuring Ultrasonic Power. *J. Acoust. Soc. Am.* (1975) 57 1436-1440
- 2 R. Reibold and W. Molkenstruck, Light Diffraction Tomography Applied to the Investigation of Ultrasonic Fields. Part I: Continuous Waves *Acustica* (1984) 56 180-192
- 3 C. V. Raman and N. Nath, Diffraction of Light by High Frequency Sound Waves *Proc. Indian Acad. Sci.* (1935) 11 406-412
- 4 Wolf, J.W. Neighbors, III, T.H. and Mayer, W.G. Optical Analysis of Finite-amplitude Ultrasonic Pulses *J. Acoust. Soc. Am.* (1990) 87 1004
- 5 Willard, G.W. *J. Acoust. Soc. Am.* (1949) 21 101-108

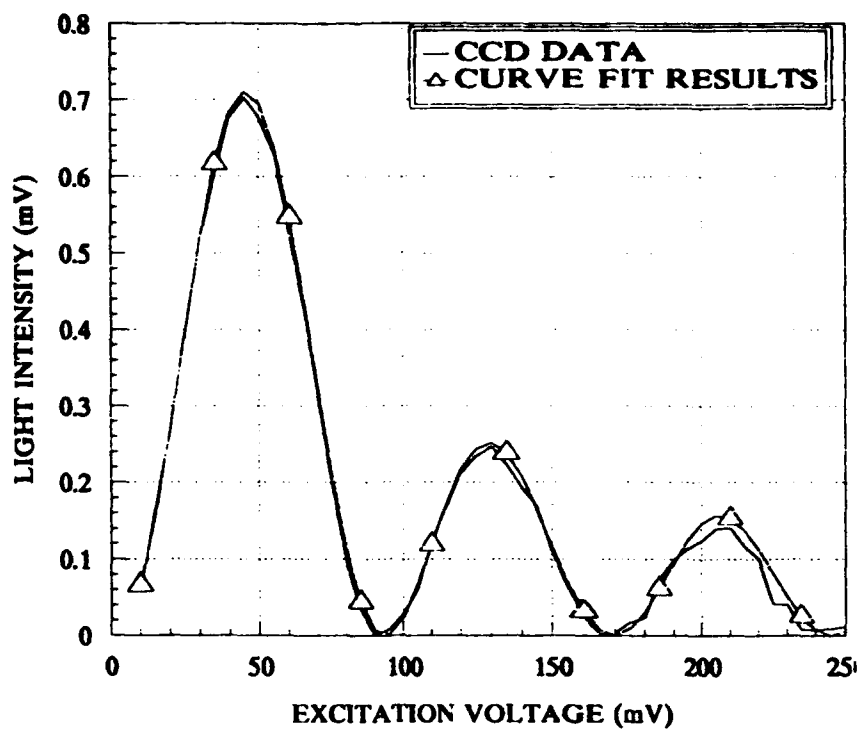


Figure 1 Light intensity vs. transducer excitation voltage

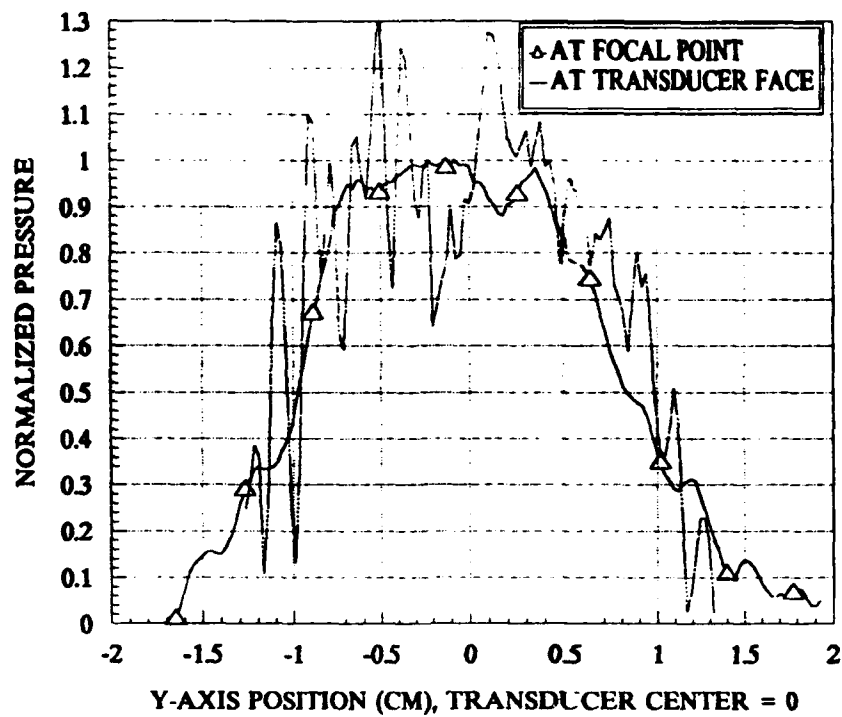


Figure 2 Pressure profile in the direction of light propagation for 30° arc transducer

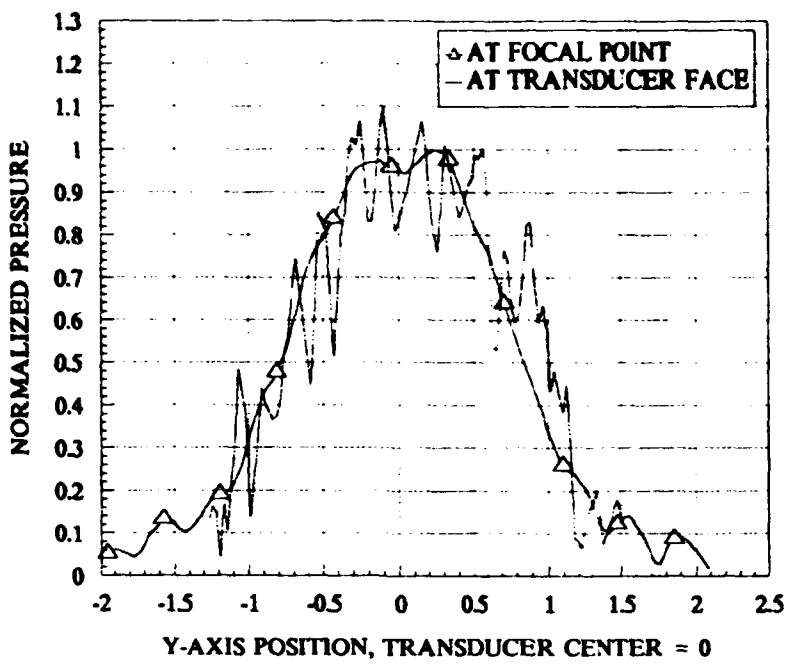


Figure 3 Pressure profile in the direction of light propagation for 60° arc transducer

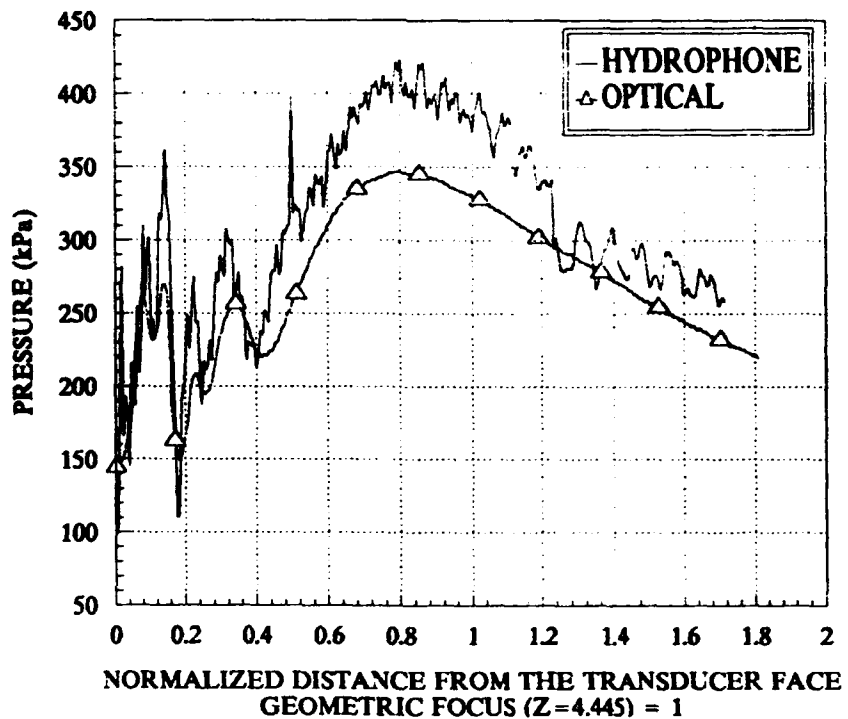


Figure 4 Pressure profile in the direction of sound propagation for 30° arc transducer

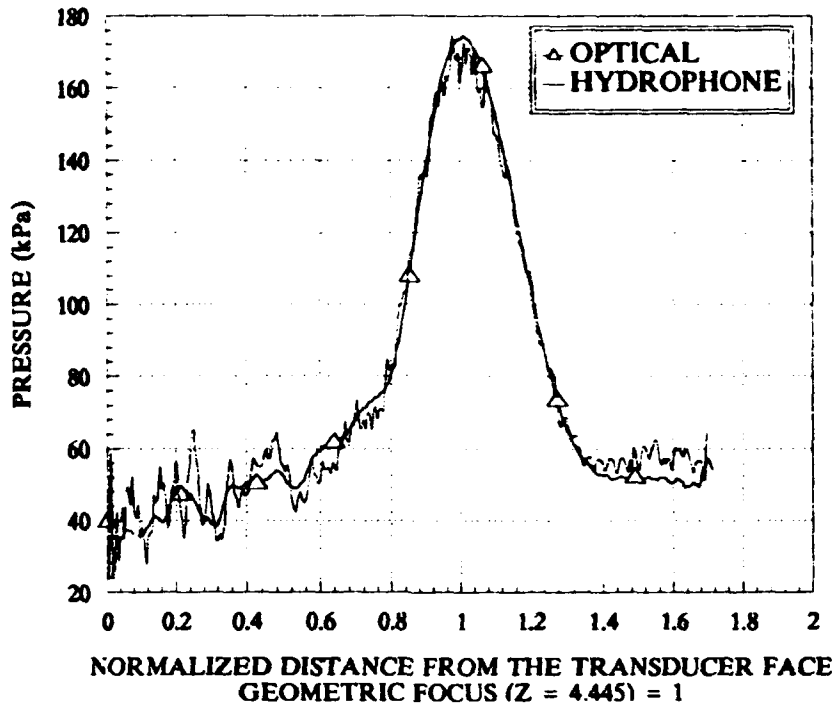


Figure 5 Pressure profile in the direction of sound propagation for 60° arc transducer

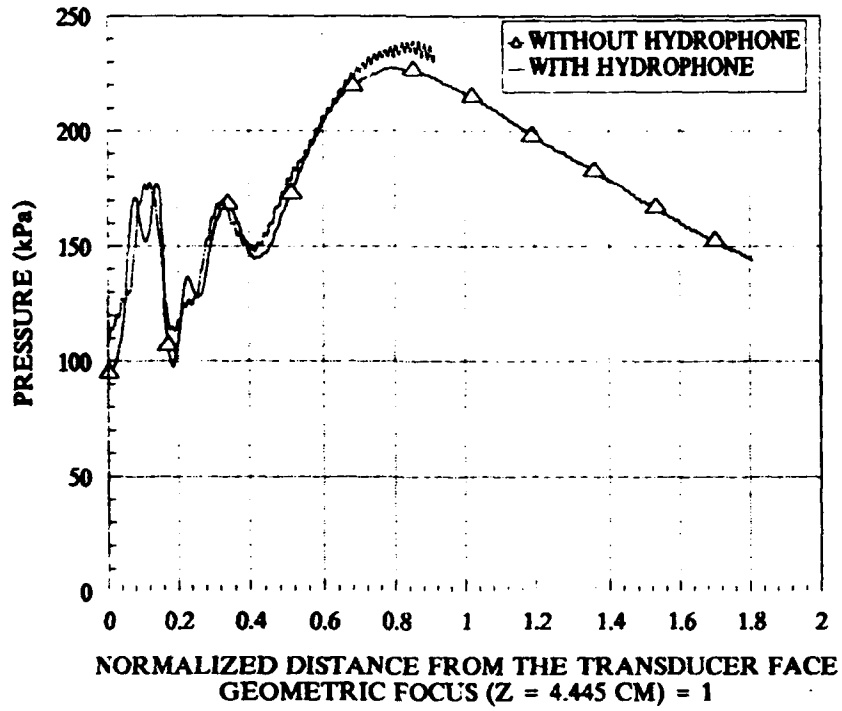


Figure 6 Pressure profiles with and without the presence of a needle hydrophone

Summary Page III

This section deals with the various advantages acousto-optic methods offer for the investigation of sound fields, particularly sound fields which are characterized by high amplitude and pulsed regimes. The main thrust of the present grant was the investigation of focused ultrasound; however, one has to realize that there are great differences between focused continuous waves and pulsed waves, particularly, as far as the mathematical description of the events is concerned.

Therefore, an investigation was undertaken to examine the possibilities of using an optical analysis of finite-amplitude ultrasonic pulses, and the feasibility of a spectral resolution of such pulses, using light diffraction by ultrasound.

This section contains reprints of two papers dealing with this topic; the author of the first paper, Dr. John Wolf, was supported by the Grant at the time. He is now a scientist at the Naval Research Laboratory in Washington, DC.

Sonderdruck aus / Reprint from

ACUSTICA

JOURNAL
INTERNATIONAL
D'ACOUSTIQUE

sous le patronage du
Groupement des Acousticiens
de Langue Française

INTERNATIONAL
JOURNAL
ON ACOUSTICS

recognized by the Institute
of Acoustics of Great Britain

INTERNATIONALE
AKUSTISCHE
ZEITSCHRIFT

unter Mitwirkung
der Deutschen
Physikalischen Gesellschaft



S. HIRZEL VERLAG · STUTTGART

Spectral Filtering of Finite Amplitude Ultrasonic Pulses by Plates. An Investigation Using Light Diffraction

J. W. Wolf, T. H. Neighbors, III, W. G. Mayer
Department of Physics, Georgetown University, Washington

Spectral Filtering of Finite Amplitude Ultrasonic Pulses by Plates. An Investigation Using Light Diffraction

Summary

Finite amplitude ultrasonic pulses, reflected and transmitted from a brass plate, are optically examined using light diffraction produced by the ultrasonic signal. Pulse Fourier spectra are derived which, when used for input to a light diffraction model, provide quantitative agreement between experiment and theory. The spectra are used in a propagation model based on Burgers' equation which describes finite amplitude acoustic waves in a nonlinear medium. Theories of ultrasonic beam reflection and transmission from plates immersed in a liquid are applied to pulsed beams and incorporated into the pulse spectrum, propagation, and light diffraction models. Examples are presented which illustrate selective filtering of pulse fundamental and harmonic frequency components by Lamb and Rayleigh mode excitation in a plate.

Spektrale Filterung von Ultraschallimpulsen endlicher Amplitude durch Platten, eine Untersuchung mit Hilfe der Lichtbeugung

Zusammenfassung

Es werden Ultraschallimpulse endlicher Amplitude, die von einer Messingplatte reflektiert und transmittiert werden mit Hilfe der vom Ultraschall hervorgerufenen Lichtbeugung optisch untersucht. Hierzu werden Fourierspektren von Impulsen abgeleitet, die, als Eingangsgröße für ein Lichtbeugungsmodell benutzt eine quantitative Übereinstimmung zwischen Experiment und Theorie ergeben. Diese Spektren werden in einem Ausbreitungsmodell verwendet, das auf der Burgersschen Gleichung zur Beschreibung von Schallwellen endlicher Amplitude in einem nichtlinearen Medium beruht. Die Theorien der Reflexion und Transmission von Ultraschallstrahlen an Platten in einer Flüssigkeit werden auf gepulste Strahlen angewandt und in die Modelle für das Pulsspektrum, die Impulsausbreitung und die Lichtbeugung eingebaut. Durch Beispiele wird die selektive Filterung der Grundfrequenz und der Harmonischen des Impulses durch Anregung von Lamb- und Rayleighwellen in der Platte demonstriert.

dell verwendet, das auf der Burgersschen Gleichung zur Beschreibung von Schallwellen endlicher Amplitude in einem nichtlinearen Medium beruht. Die Theorien der Reflexion und Transmission von Ultraschallstrahlen an Platten in einer Flüssigkeit werden auf gepulste Strahlen angewandt und in die Modelle für das Pulsspektrum, die Impulsausbreitung und die Lichtbeugung eingebaut. Durch Beispiele wird die selektive Filterung der Grundfrequenz und der Harmonischen des Impulses durch Anregung von Lamb- und Rayleighwellen in der Platte demonstriert.

Etude, par la diffraction de la lumière, du filtrage spectral d'impulsions ultrasonores d'amplitude finie par des plaques solides

Sommaire

On a examiné optiquement la lumière diffractée par le signal ultrasonore réfléchi ou transmis par une plaque de laiton insonnée par des impulsions acoustiques d'amplitudes finies. Parallèlement on a calculé les spectres de Fourier pour les impulsions et on les a utilisés comme signaux d'entrée dans un modèle de diffraction acoustique de la lumière, obtenant ainsi un accord quantitatif entre calculs et expériences. Le modèle propagatif utilisé repose sur l'équation de Burgers décrivant la propagation d'ondes acoustiques d'amplitude finie dans un milieu non linéaire. Puis on a appliqué à des faisceaux pulsés les théories connues de la réflexion et de la transmission d'un faisceau d'ultrasons par une plaque immergée dans un liquide et on les a incorporées dans des modèles composites englobant spectres d'impulsions, propagations et diffraction de la lumière. Enfin on présente des exemples illustrant le filtrage sélectif des composantes spectrales fondamentales et harmoniques des impulsions par les modes de Lamb et de Rayleigh excités dans la plaque.

Introduction

Light diffraction has been used effectively as a tool for in-situ measurements of ultrasonic fields since the phenomenon was first observed by Lucas and Biquard [1] and Debye and Sears [2], and explained by the Raman and Nath [3] theory in the 1930's. By the late 1950's,

Raman-Nath diffraction was successfully used to probe continuous wave (CW) finite amplitude ultrasonic beams [4]. Ten years later the basic Raman-Nath theory was generalized to account for light sources with Gaussian intensity distributions [5] and the consideration of pulsed rather than CW ultrasound [6]. Motivated by experimental observations in the early 1980's [7], Raman-Nath diffraction theory was extended to account for arbitrary pulsed ultrasonic waveforms [8].

Recently an experimental apparatus was developed using a long optical path with which one can examine a large variety of ultrasonic pulses [9]. The apparatus

Received 30 May 1989,
accepted 31 December 1989.

Dr. J. W. Wolf, T. H. Neighbors, III, Prof. W. G. Mayer,
Ultrasonics Research Laboratory, Department of Physics,
Georgetown University, Washington, D.C. 20057 USA.

is first used to characterize transducer frequency response to CW excitation. The empirical results are used with a computer algorithm to construct a model of pulse Fourier spectra as a function of pulse duration, repetition and centre frequencies. The technique adequately models pulses at the transducer element in the liquid. Mayer and Neighbors [10] combined the pulse light diffraction theory with a model of acoustic wave propagation in nonlinear media [11]. In their paper, they suggested the use of light diffraction for estimating the magnitude of harmonic distortion in finite amplitude ultrasonic pulses. The distortion appears as asymmetries in theoretical pulse light diffraction pattern intensity distributions. The optical system was used to examine finite amplitude pulse harmonic growth yielding results that agreed with theoretical predictions [12]. These preliminary studies [9, 12] have shown the utility of the diffraction apparatus for characterizing ultrasonic pulses and examining changes in the pulse spectrum due to medium nonlinearities.

The present paper is concerned with the optical analysis of pulsed ultrasonic beams before and after reflection and transmission from a solid plate immersed in the liquid medium. A satisfactory theoretical description of ultrasonic beam reflection from plates was provided by Pitts, Plona and Mayer [13] where they analyzed the plane wave reflection coefficient and revealed the conditions necessary for an ultrasonic beam to generate vibrational modes in the plate.

Assume a monochromatic ultrasonic beam is incident at some angle upon a plate while its amplitude is continuously monitored at a fixed location beyond the reflecting surface and along the beam axis. If the incidence angle is changed to a mode critical angle, measurement would show a decrease in the beam amplitude because part of the beam energy would no longer be geometrically reflected from the plate. If the incident beam was polychromatic, such as a train of ultrasonic pulses consisting of a discrete frequency spectrum, a measurement of the reflected beam would show an amplitude decrease in those pulse frequency components that individually satisfy the conditions of plate mode conversion. Correspondingly, a transmitted pulse train will contain those amplitude terms that originated from the incident pulse spectrum and were removed from the reflected spectrum by mode conversion. The plate acts as a frequency filter. From this description, it is obvious that, for a particular plate, the frequency spectra of the reflected and transmitted pulse may be significantly different from the incident pulse Fourier spectrum. If monitored with a light beam, changes in pulse amplitude spectra could be directly measured from changes in the intensity

distribution of the light diffraction pattern produced by these pulses.

The sections that follow: (1) describe the experimental apparatus; (2) summarize the relevant aspects of pulse modeling and light diffraction by pulsed ultrasound; (3) look at a model of high amplitude pulse propagation in nonlinear media; (4) review the theory of pulse reflection and transmission from plates; (5) demonstrate the use of the pulse propagation and reflection models; and (6) provide observations of spectral filtering in experimental light diffraction patterns. A more detailed description of the experimental apparatus, procedures and theoretical models used for this study can be found in the references [8–13].

Experimental apparatus

The light diffraction apparatus can resolve light diffraction patterns produced by pulses with repetition frequencies as low as 40 kHz [9]. The system uses cylindrical lenses which produce a light beam of linear cross section that interacts with a slice of the ultrasonic beam along its symmetry axis. A transducer of 2.2 cm diameter produces the ultrasonic beam which is intersected normally by the light beam within a water tank. The resulting diffraction pattern is measured by a photomultiplier tube light detector. The signal input to the ultrasonic transducer is driven from the amplified output of a pulse function generator. A computer operated data acquisition system controls the light detector and pulse function generator.

Pulse model and light diffraction theory

A model of ultrasonic pulse spectra at the source in the liquid is based on a measured ultrasonic amplitude transfer as a function of frequency, $\tau_1(f)$; for this study from a nominal 1 MHz transducer [9]. In the pulse mode, the function generator introduces ideal signals to the transducer which are characterized by pulse centre and repetition frequencies, f_0 and f_p , respectively, and burst number, which is related to pulse duration. Theoretical pulse spectra are constructed from a discrete convolution of the electronic signal amplitude spectrum with $\tau_1(f)$. The resulting spectrum is used as input to the light diffraction model and is expressed as a Fourier sine expansion

$$v(x, t) = v \sum_{n=0}^{\infty} a_n \sin[n(\omega_p t - k_p x) + \phi_n], \quad (1)$$

where $\omega_p = 2\pi f_p$, $k_p = 2\pi/\lambda_p$, λ_p = the pulse wavelength in the medium and v , the Raman-Nath param-

eter [3], is proportional to the pulse peak amplitude. The a_n and ϕ_n are, respectively, the amplitude and phase of the n^{th} Fourier component of the pulse. The light intensity distribution as a function of diffraction angle θ is given by [8]

$$I(\theta) = \sum_{m=-\infty}^{\infty} I_m [\sin(k \sin \theta - m k_p)/(k \sin \theta - m k_p)]^2, \quad (2)$$

where:

$$I_m = \left| \sum_{r_2=-\infty}^{\infty} \dots \sum_{r_n=-\infty}^{\infty} J_{r_1(m)}(v_1) \dots J_{r_n}(v_n) \dots \exp[i(r_1(m)\phi_1 + \dots + r_n\phi_n + \dots)] \right|^2,$$

$$r_1(m) = m - 2r_2 - \dots - nr_n - \dots,$$

$k = 2\pi/\lambda$, $v_n = v a_n$, and J_r is the Bessel function of order r . Eq. (2) represents a diffraction pattern which exhibits distinct maxima when

$$\sin \theta_m = \pm \lambda/k_p. \quad (3)$$

Model of nonlinear pulse propagation

The pulse propagation theory is based on a modified form of Burgers' equation to describe acoustic wave distortion due to medium nonlinearities. The model expresses the incremental change of the n^{th} harmonic component of the pulse particle velocity, U_n , by [11]

$$U_n(x+dx) = U_n(x) + \left\{ (i\beta \omega_p/c^2) \left[\sum_{j=1}^n j U_j U_{n-j} + \sum_{j=n+1}^{\infty} n U_j U_{j-n}^* \right] - \alpha n^2 U_n \right\} dx \quad (4)$$

where: dx is the incremental distance, $\beta = 1 + (B/2A)$ the medium nonlinearity parameter, c the sound velocity, α the medium attenuation coefficient and $*$ indicates the complex conjugate. The use of this model will be demonstrated in a different section of this paper.

Theoretical pulse reflection and transmission from a plate

The geometry of the pulse-plate interaction is illustrated in Fig. 1. Within a liquid, an ultrasonic pulse is incident at an angle Θ_i upon a solid plate of thickness D . To describe the interaction, the monochromatic formulation is applied to pulses by multiplying each of the incident pulse spectral components by the appropriate reflection or transmission coefficient. The coefficients, $R(k_x)$ and $T(k_x)$, respectively, are complex functions of $k_x = k_0 \sin \Theta_i$, the wave vector compo-

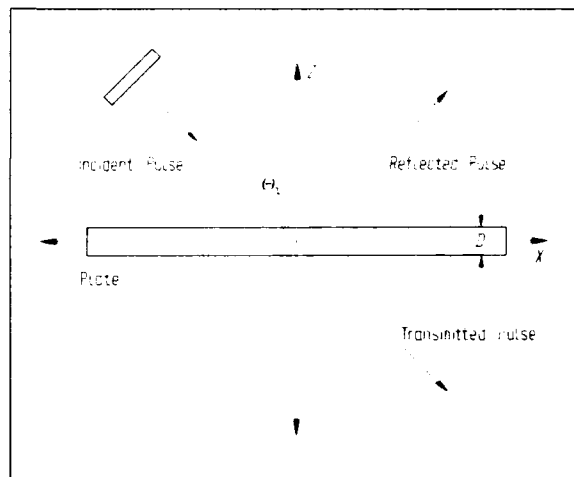


Fig. 1. Geometry of the pulse-plate interaction.

ment along the liquid-plate interface, with k_0 the incident wave number in the liquid. Pitts et al. [13] define the plane wave reflection coefficient

$$R(k_x) = N/[F_a F_s], \quad (5)$$

with the definitions:

$$F_a = [k_s^2 - 2k_x^2]^2 [1 - \cos P]/\sin P + 4k_x^2 \chi_s \chi_d [1 - \cos Q]/\sin Q + i\varrho k_s^4 \chi_d/\chi,$$

$$F_s = [k_s^2 - 2k_x^2]^2 [1 + \cos P]/\sin P + 4k_x^2 \chi_s \chi_d [1 + \cos Q]/\sin Q - i\varrho k_s^4 \chi_d/\chi,$$

$$N = [k_s^2 - 2k_x^2]^4 + 16k_x^4 \chi_s^2 \chi_d^2 - \varrho^2 k_s^8 \chi_d^2/\chi^2 + 8[k_s^2 - 2k_x^2]^2 k_x^2 \chi_s \chi_d [1 - \cos P \cos Q]/[\sin P \sin Q].$$

$\chi_s = k_0 [(c_0/c_s)^2 - \sin^2 \Theta_i]^{1/2}$, $\chi_d = k_0 [(c_0/c_d)^2 - \sin^2 \Theta_i]^{1/2}$, $k = k_0 \cos \Theta_i$, $P = D \chi_d$, $Q = D \chi_s$ and $\varrho = \varrho$ (liquid)/ ϱ (solid), the ratio of the medium densities. The values c_s and c_d are the shear and compressional wave velocities of sound in the solid, respectively. The plane wave transmission coefficient is given [13] by:

$$T(k_x) = \{2i\varrho k_s^4 \chi_d/\chi\} \{[k_s^2 - 2k_x^2]^2/\sin P + 4k_x^2 \chi_s \chi_d/\sin Q\}/[F_a F_s]. \quad (6)$$

With measured values for c , c_s , c_d , ϱ (liquid) and ϱ (solid), the two coefficients reduce to functions of $f = c/2\pi k_0$, D and Θ_i . Since the frequency, f , and plate thickness, D , are coupled in the expressions, $R(k_x)$ and $T(k_x)$ reduce to functions of fD and Θ_i . The subscripts, a and s , of the functions F in eqs. (5) and (6) refer to the antisymmetric and symmetric vibrational modes of the plate as defined in the references [14]. When either $F_a = 0$ or $F_s = 0$, the functions $R(k_x)$ and $T(k_x)$ produce so-called pole-zero pairs which define the conditions giving rise to Lamb mode conversion of the incident beam energy [13].

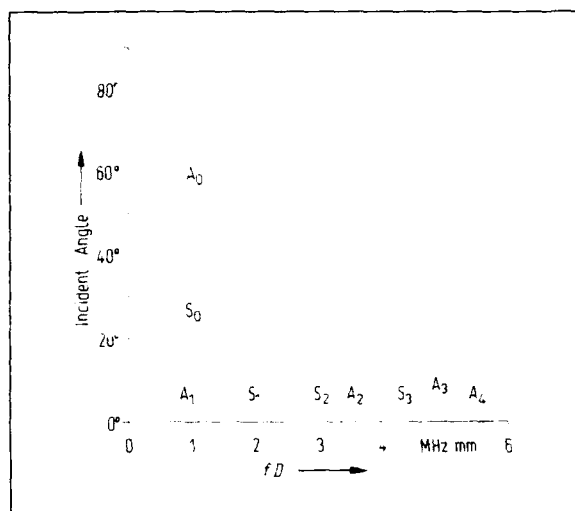


Fig. 2. Set of velocity dispersion curves for a brass plate in water with characteristic values listed in Tables I and II.

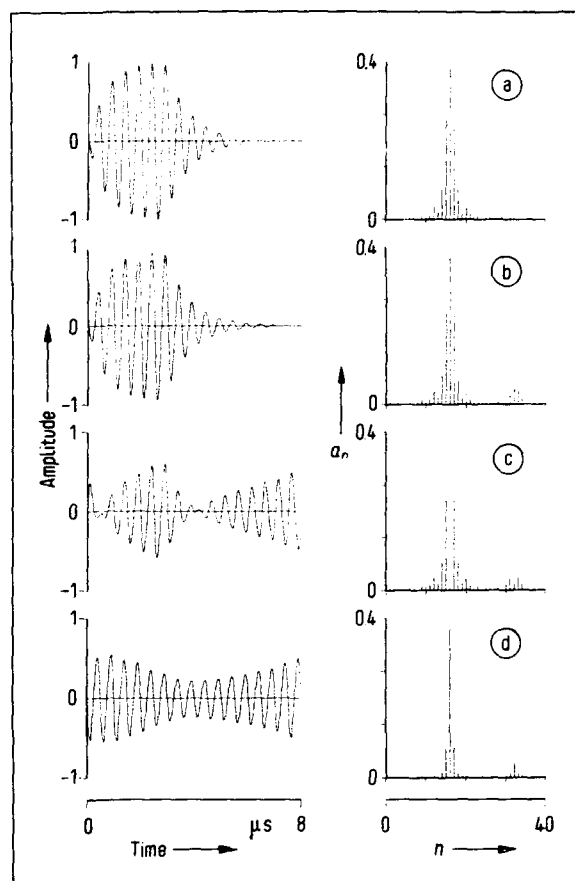


Fig. 3. Time history and Fourier amplitude spectrum of a pulse with $f_0 = 2.0$ MHz, $f_p = 125.0$ kHz, exponential rise and decay time of 0.85 μ s and $u_0 = 3.0$ cm/s; a) prior to propagation; b) after propagating 50 cm in water with medium values listed in Table I; c) reflected from a brass plate with $D = 1.69$ cm at a Lamb mode critical angle of $\Theta_i = 30^\circ$; and d) transmitted from the plate.

Table I. Measured characteristics for water.

$$\begin{aligned} \rho &= 1.0 \text{ g cm}^{-3} \\ c &= 1487.9 \text{ m s}^{-1} (T = 22^\circ \text{ C}) [15] \\ B/A &= 5.2 [16] \\ x &= x' f^2, x' = 2.5 \times 10^{-14} \text{ Np s}^2 \cdot \text{m} [17] \end{aligned}$$

Table II. Measured characteristics for brass.

$$\begin{aligned} \rho &= 8.5 \text{ g cm}^{-3} \\ c_s &= 2240.0 \text{ m s}^{-1} [18] \\ c_d &= 4781.0 \text{ m s}^{-1} [18] \end{aligned}$$

Fig. 2 shows a set of velocity dispersion curves of plate modes as a function of critical angles of incidence and the product fD , calculated with the measured values listed in Table II for a brass plate immersed in water. The curves represent the solutions of $F_x = 0$ or $F_y = 0$ for real k_x and are labeled A_0 , S_0 , A_1 , etc., to distinguish the antisymmetric and symmetric plate modes of vibration. These curves serve as a guide for selective filtering of frequencies in pulse spectra.

A sample run

For demonstration, a theoretical pulse train is constructed with an initial peak amplitude $u_0 = 3.0$ cm/s, $f_0 = 2.0$ MHz, $f_p = 125.0$ kHz, and an exponential rise and decay time of 0.85 μ s. The pulse travels within the propagation model a distance of $x = 50$ cm in water using medium parameters listed in Table I. The top two sets of graphs in Fig. 3 show the normalized time history and amplitude spectrum of the initial (a) and propagated (b) pulse where one sees a significant amount of harmonic growth.

The pulse is now assumed incident at $\Theta_i = 30^\circ$ upon a brass plate of thickness $D = 1.69$ mm. The pulse centre frequency and plate thickness provide an fD value of 3.38 MHz · mm which places the pulse fundamental frequencies across the A_1 plate mode, (see Fig. 2). Fig. 3 shows the resulting reflected (c) and transmitted (d) pulse time histories and amplitude spectra. The incident pulse is highly distorted by reflection since several frequency terms have been filtered from its spectrum including harmonics filtered by other plate modes, S_2 , A_2 , etc. Frequency terms from the incident pulse spectrum which were filtered from the reflected wave appear in the transmitted pulse spectrum.

The dispersion curves of Fig. 2 indicate that the A_0 and S_0 curves merge resulting in a large region of frequency bandpass for the plate. Fig. 4 illustrates the reflected (top) and transmitted (bottom) pulse result-

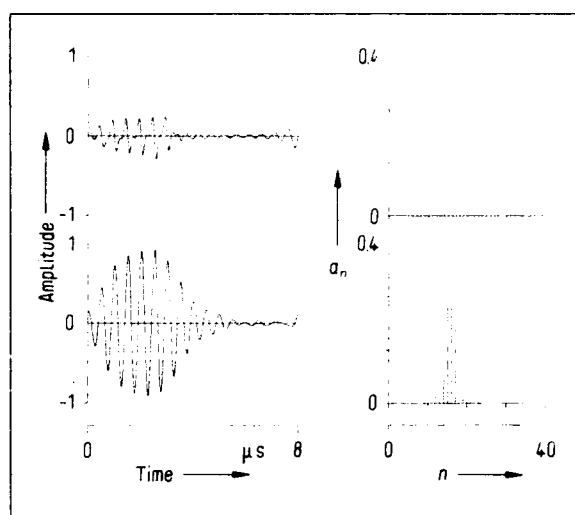


Fig. 4. Time history and Fourier amplitude spectrum of the finite amplitude pulse of Fig. 3b reflected (top) and transmitted (bottom) from a brass plate at a Rayleigh mode critical angle of $\Theta_i = 45^\circ$.

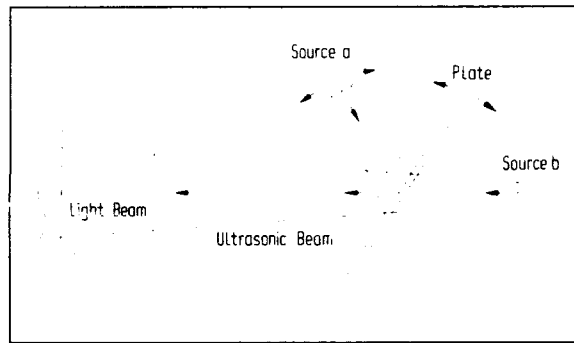


Fig. 5. Ultrasonic beam configuration for the two cases of beam reflection (Source a) and transmission (Source b) from a plate.

ing from the theoretical pulse of Fig. 3 incident upon the brass plate at $\Theta_i = 45^\circ$ which excites a Rayleigh type plate mode [13]. The reflected pulse spectrum has a greater percentage content of higher harmonics than the incident pulse. The transmitted pulse spectrum indicates that almost all higher harmonics within the incident spectrum have been filtered by the plate. The transmitted pulse time history shows little indication, except for dissipative losses, of finite amplitude distortion and, essentially, only the initial pulse frequencies are present.

Observation of spectral filtering by light diffraction

The actual orientation of the ultrasonic source, plate, and light beam in the water tank for analysis of pulsed

beams is illustrated in Fig. 5 for the case of pulses (a) reflected and (b) transmitted from the plate. Once the pulse-plate configuration is chosen, the data acquisition system digitizes the light diffraction pattern produced by the acoustooptic interaction.

Fig. 6 presents experimental light diffraction patterns (left) and those predicted by the combined pulse spectrum, propagation, reflection and light diffraction models (right). The initial pulse was produced by a nominal 1 MHz source and was modeled using $\tau_1(f)$ and the values $f_p = 132.2$ kHz, $f_0 = 0.925$ MHz, burst number 2, output amplitude $u_0 = 3.56$ cm/s and $v = 1.45$. The first light pattern set was produced by the finite amplitude pulse, travelling 40 cm without plate interaction. The difference in intensity between the second set of positive and negative satellite diffraction orders, $I_{\pm 13}$, $I_{\pm 14}$ and $I_{\pm 15}$, ($f = 1.719$, 1.851 and 1.983 MHz), is due to propagation-induced harmonic generation. It is this light intensity asymmetry from which one can estimate the level of harmonic distortion in finite amplitude pulses [10, 12]. For the other three light pattern sets, a brass plate was mounted 11.5 cm from the source so that ultrasonic pulses are reflected from the plate into the light interaction region while a total travel distance of 40 cm is maintained, (see Fig. 5a). The plate thickness, $D = 3.16$ mm, and the pulse centre frequency, $f_0 = 925.4$ kHz yield an $fD = 2.923$ MHz · mm. The light diffraction patterns result from incident angles of $\Theta_i = 25^\circ$, 28° , and 32° where the dominant pulse spectral terms pass through the brass by excitation of the plate's A_1 Lamb mode (see Fig. 2). Each pattern indicates that a different spectral term has been filtered from the incident pulse spectrum.

Compare the top set of light patterns in Fig. 6 to the bottom three. For $\Theta_i = 25^\circ$, reflection introduces an intensity decrease in the $I_{\pm 6}$ diffraction orders which corresponds to the $n = 6$ spectral term of the pulse ($f = 793.2$ kHz). Looking toward diffraction orders corresponding to pulse harmonics, one sees the $I_{\pm 13}$ has decreased to below the measurement threshold of the apparatus because a large contribution to its intensity is $I_{\pm 6}$. The remaining orders, $I_{\pm 14}$ and $I_{\pm 15}$ continue to show asymmetry with respect to I_0 indicating harmonics are still present in the pulse spectrum. The orders centred about I_0 , that is $I_{\pm 1}$, decrease since the largest contribution to their intensity comes from the pulse spectral terms that were removed by the plate.

Since it has a positive slope, the A_1 mode passes upward through the pulse spectrum as the incident angle is increased. In the pattern set for $\Theta_i = 28^\circ$, the light order corresponding to the pulse centre frequency, $I_{\pm 7}$ ($f = 925.4$ kHz), has dropped almost an order of magnitude in intensity causing the $I_{\pm 13}$, $I_{\pm 14}$ and

$I_{\pm 15}$ to decrease below the apparatus measurement threshold. The remaining $I_{\pm 1}$ diffraction orders in the measured pattern, are caused by slit diffraction within the optical apparatus. In the set for $\Theta_i = 32^\circ$, the $n = 8$ pulse spectral term has been filtered by the plate, removing the $I_{\pm 8}$ ($f = 1.058$ MHz) and the $I_{\pm 15}$ orders from the diffraction pattern.

Fig. 7 compares the measured light patterns of Fig. 6 produced by the reflected pulses (left) to measured patterns produced by the incident pulse transmitted through the same plate at corresponding Θ_i (right), (see Fig. 5 b). In each of the three cases, the patterns indicate that spectral terms filtered by plate reflection appear in the transmitted pulse spectrum. The second light pattern set shows the transmitted spectrum describes an almost monochromatic ultrasonic beam where the plate has transformed a pulsed

wave (interacting with the plate only part of the time) into a quasi-continuous wave. Through mode conversion, the plate continues ringing after the incident beam is no longer exciting it, thereby broadening the pulse train almost into a CW beam.

The apparatus was also used to illustrate selective filtering of harmonics generated by finite amplitude ultrasound propagation as was done theoretically in the sample run. Fig. 8 presents two measured diffraction patterns produced by a transmitted pulsed beam, originally incident on the brass plate at a critical Rayleigh mode angle of $\Theta_i = 45^\circ$. The resulting light patterns indicate that the fundamental spectral components of the pulse were transmitted through the plate. In the top graph of Fig. 8, the intensity asymmetry of the $I_{\pm 13}$, $I_{\pm 14}$ and $I_{\pm 15}$ diffraction orders indicates the presence of harmonics which result from the pulse propagating an additional 28.2 cm beyond the plate to the light beam.

To demonstrate harmonic filtering, the brass plate was positioned closer to the light beam while keeping the total pulse propagation distance the same. In the bottom diffraction pattern of Fig. 8, one can see the diffraction orders are symmetrical with respect to I_0 .

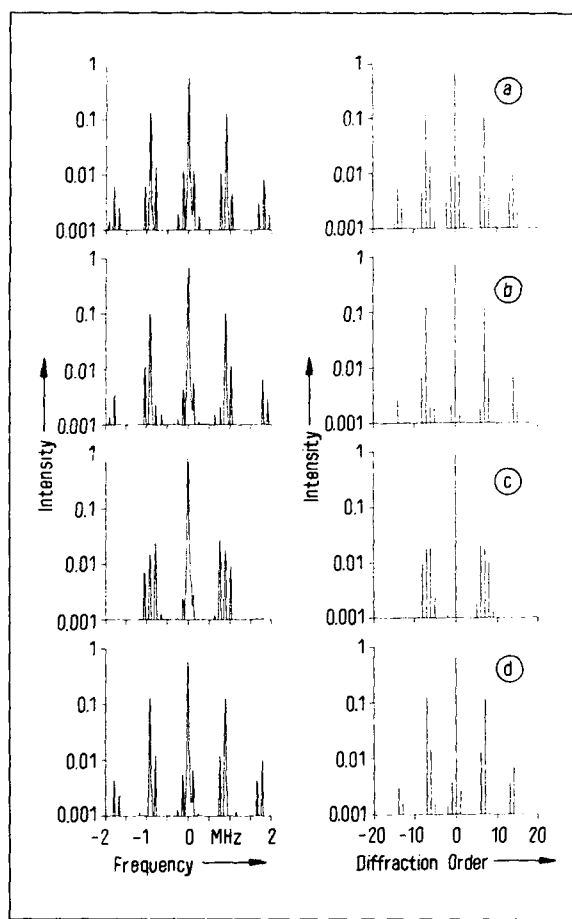


Fig. 6. Measured (left) and modelled (right) light diffraction patterns produced by a finite amplitude pulse with total propagation $x = 40$ cm. The top pattern set is of the pulse without a plate (a) and the others are reflected from a brass plate at position $x = 11.5$ cm, with $\Theta_i = 25^\circ$ (b), 28° (c) and 32° (d).

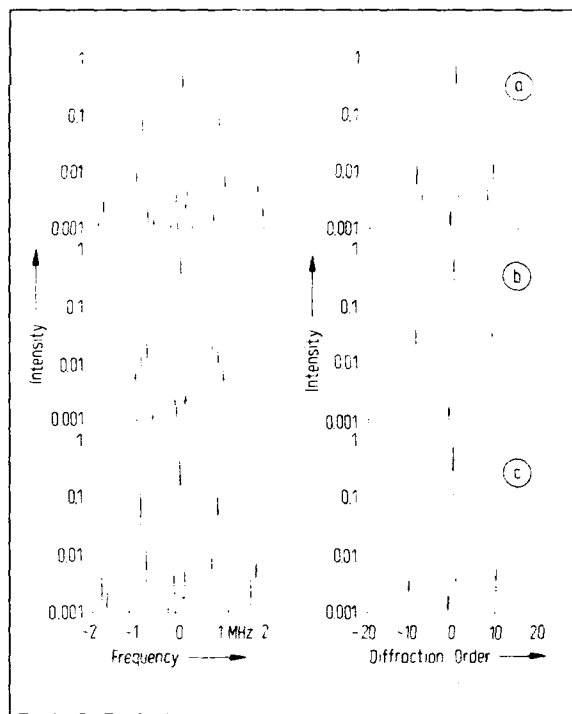


Fig. 7. Measured light diffraction patterns produced by the pulse-plate configuration of Fig. 6. The left patterns are of the reflected pulse and the right are of the transmitted pulse. $\Theta_i = 25^\circ$ (a), 28° (b) and 32° (c).

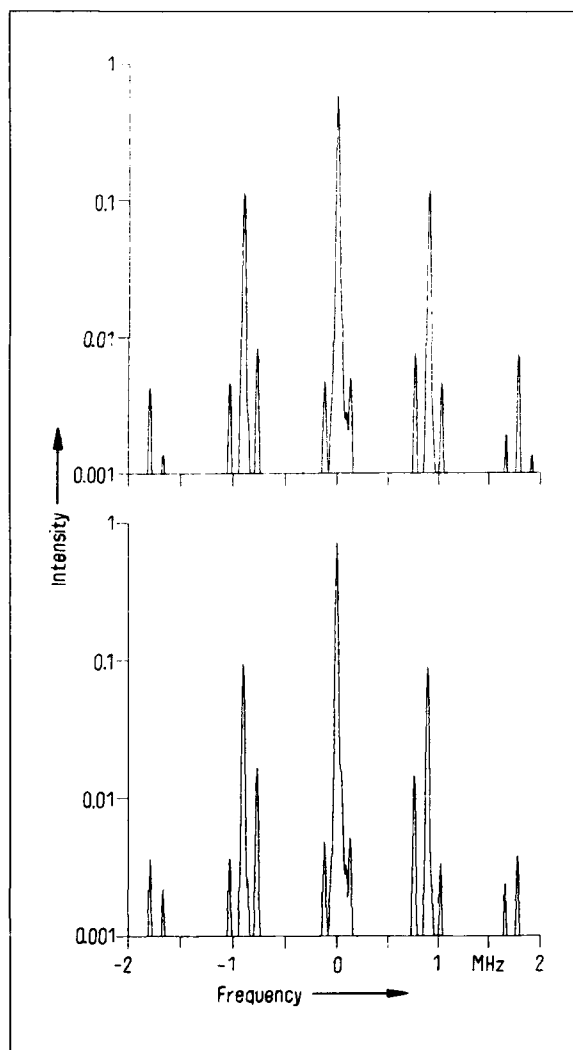


Fig. 8. Measured diffraction patterns produced by the transmitted pulse originally incident upon the brass plate at $\Theta_i = 45^\circ$. The plate is located at $x = 11.5$ cm (top) and $x = 28.5$ cm (bottom).

indicating the plate has filtered the harmonic terms in the pulse spectrum. The plate has effectively removed the harmonic distortion of the finite amplitude pulse.

Conclusions

The experimental apparatus has been used to examine noninvasively finite amplitude ultrasonic pulses reflected and transmitted from plates in a nonlinear liquid. The theory describing reflection and transmission from plates has been combined with the pulse spec-

trum, propagation and light diffraction models. The complete model predicts pulsed ultrasonic beam spectral filtering by plates immersed in liquids, which was then verified experimentally with the light diffraction apparatus. By examining its dispersion curve, it has been shown that a solid plate can be used to filter selected frequencies of a pulse spectrum, such as individual components or whole regions of the spectrum. The results demonstrate the application of light diffraction to analysis of ultrasonic pulses and their interaction with both the propagation medium and solid materials within it. The technique has the advantage of performing an effective spectral analysis of an ultrasonic beam with a minimum of signal processing and virtually no measurable distortion of the ultrasonic field.

Acknowledgement

This work was supported by the Office of Naval Research, U.S. Navy. Partial financial support by NATO Scientific Affairs Division is gratefully acknowledged by two of the authors (T. H. N. and W. G. M.).

References

- [1] Lucas, R. and Biquard, P., *C. R. Acad. Sci. (Paris)* **195** [1932], 121.
- [2] Debye, P. and Sears, F. W., *Proc. Natl. Acad. Sci. USA* **18** [1932], 63.
- [3] Raman, C. V. and Nath, N. S. N., *Proc. Ind. Acad. Sci. A* **2** [1935], 406.
- [4] Zankel, K. L. and Hiedemann, E. A., *J. Acoust. Soc. Amer.* **31** [1959], 44.
- [5] Hargrove, L. E., *J. Acoust. Soc. Amer.* **43** [1968], 847.
- [6] Zitter, R. N., *J. Acoust. Soc. Amer.* **43** [1968], 864.
- [7] Häusler, E., Mayer, W. G., and Schwartz, M., *Acoust. Lett.* **4** [1981], 180.
- [8] Neighbors, T. H., III and Mayer, W. G., *J. Acoust. Soc. Amer.* **74** [1983], 146.
- [9] Wolf, J. W., Neighbors, T. H., III, and Mayer, W. G., *Ultrasonics* **27** [1989], 150.
- [10] Mayer, W. G. and Neighbors, T. H., III, *Ultrasonics* **25** [1987], 83.
- [11] Haran, M. E. and Cook, B. D., *J. Acoust. Soc. Amer.* **73** [1983], 774.
- [12] Wolf, J. W., Neighbors, T. H., III, and Mayer, W. G., *J. Acoust. Soc. Amer.* **87** [1990], 1004.
- [13] Pitts, L. E., Plona, T. J., and Mayer, W. G., *IEEE Trans. Sonics Ultrason.* **SU-24** [1977], 101.
- [14] Brekhovskikh, L. M., *Waves in layered media*. Academic Press, New York 1960.
- [15] Medwin, H., *J. Acoust. Soc. Amer.* **58** [1975], 1318.
- [16] Kashkooli, H. A., Dolan, P. J., Jr., and Smith, C. W., *J. Acoust. Soc. Amer.* **82** [1987], 2086.
- [17] Pinkerton, J. M. M., *Nature* **160** [1947], 128.
- [18] Wolf, J., Ngoc, T. D. K., Kille, R., and Mayer, W. G., *J. Acoust. Soc. Amer.* **83** [1988], 122.

Optical analysis of finite-amplitude ultrasonic pulses

J. W. Wolf, T. H. Neighbors, III,^{a)} and W. G. Mayer

Ultrasonic Research Laboratory, Department of Physics, Georgetown University, Washington, DC 20057

(Received 20 January 1989; accepted for publication 18 September 1989)

Finite-amplitude pulses are examined acousto-optically using a newly developed light-diffraction apparatus. Based on an optical analysis of ultrasonic transducer response to continuous-wave excitation at and near the fundamental frequency, pulse Fourier spectra are derived for input to a light-diffraction model, providing quantitative agreement between experiment and theory. The diffraction theory predicts that a light-diffraction pattern produced by a harmonically distorted acoustic pulse train will exhibit asymmetry in the intensity distribution with respect to the zero order. To simulate harmonic distortion, pulse frequency spectra are used for input to a computational model that is based on the Burgers' equation for propagation of finite-amplitude acoustic waves in a nonlinear medium. The spectrum, propagation, and light-diffraction models give a complete description of light diffraction by finite-amplitude pulses and provide good agreement with experimentally obtained diffraction patterns.

PACS numbers: 43.25.Zx

INTRODUCTION

Since initial experimental observations of light diffraction by ultrasonic waves^{1,2} and the subsequent theoretical explanation of these observations by Raman and Nath³ in the 1930s, light diffraction has been an effective tool for *in situ* measurements of ultrasonic fields. In the late 1950s, Raman-Nath diffraction was successfully used for the optical probing of finite-amplitude continuous-wave propagation, providing direct measurements of harmonic components.⁴

In the late 1960s the basic Raman-Nath theory was generalized to account for light sources with Gaussian intensity distributions⁵ and the consideration of pulsed rather than monochromatic ultrasound.⁶ Initial experimental observations were made of light-diffraction patterns using pulsed ultrasound,⁷ and based on these observations, the Raman-Nath diffraction theory has been generalized by Neighbors and Mayer⁸ to account for arbitrary ultrasonic waveforms. In another paper, Mayer and Neighbors⁹ proposed a technique for estimating harmonic generation in finite-amplitude ultrasonic pulses by examining their light-diffraction patterns.

Recently, an experimental apparatus has been developed using a long optical path which allows one to examine a broad range of ultrasonic pulse waveforms. The results obtained have validated the generalization of the Raman-Nath theory to arbitrary pulse shapes.¹⁰ The apparatus first analyzes transducer response to continuous-wave-mode excitation (cw) that is used to predict the structure of pulse Fourier spectra as a function of their duration, repetition, and center frequencies. The technique provides a quantitative agreement of the pulse diffraction theory with actual diffraction patterns.

This paper presents a comparison of experimental diffraction patterns produced by finite-amplitude ultrasonic pulses with the predictions of pulsed ultrasound diffraction

theory. The experimental observations provide an indirect noninteractive technique for observing growth and decay of harmonic components. Previous experimental observations by Zankel and Hiedemann,⁴ in examining the diffraction patterns produced by initially monochromatic, finite amplitude ultrasound (for example, cw beams), showed that the generation of harmonics in the ultrasonic field produced an asymmetry about the central diffraction order. The current experimental observations show the same trends for pulses and demonstrate the practical application of light diffraction to analysis of ultrasonic pulsed fields in nonlinear media.

The sections that follow (1) outline the experimental setup; (2) describe the procedure used to characterize the pulse prior to any significant effects of propagation based on transducer output characteristics and summarize the relevant aspects of pulsed ultrasound diffraction theory; and (3) introduce the finite-amplitude-pulse characteristics into this theory and illustrate the experimental observation of harmonic growth in finite-amplitude pulse propagation. A detailed description of the experimental apparatus and the pulsed ultrasound diffraction theory can be found in the references.⁸⁻¹⁰

I. EXPERIMENTAL APPARATUS

Figure 1 is a drawing of the light-diffraction apparatus that uses He-Ne laser light with $\lambda = 632.8$ nm and accommodates a light beam with an object-to-image plane distance of 7 m and width of 9 cm. A cylindrical lens diverges the light beam in one dimension only, allowing all the laser light to pass through the acoustic beam, ensuring proper normalization of a diffraction pattern. The acousto-optic interaction takes place within a channel of 4.5-cm width, bounded by glass windows, allowing the light beam to intersect normal to the ultrasonic beam within the interaction vessel. The transducer is an air-backed mounted PZT crystal of 2.5 cm in diameter. It is driven from the output of an rf power amplifier that receives an input signal from a computer-con-

^{a)}Permanent address: Falcon Associates, 6862 Elm St., McLean, VA 22101.

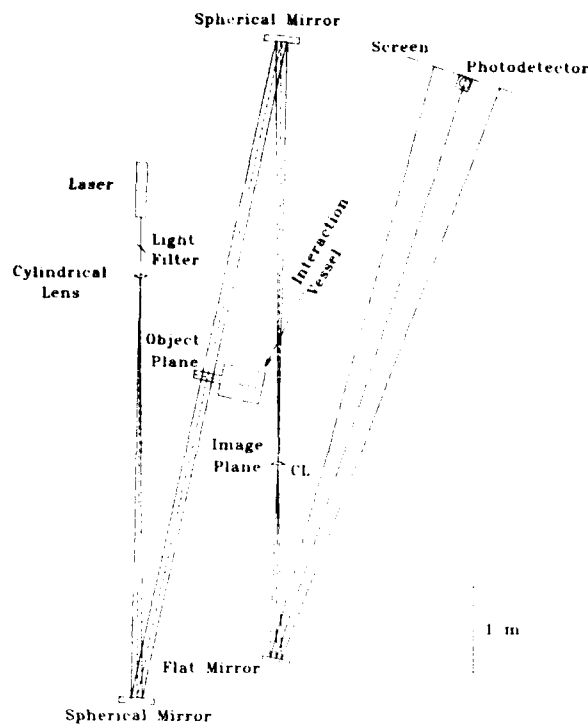


FIG. 1. Schematic of experimental system, approximately to scale.

trolled pulse function generator. Acoustic absorbing rubber is placed at the end of the channel to prevent reflections, permitting only progressive ultrasonic waves to interact with the light. Beyond the interaction vessel a second cylindrical lens collimates the diffracted light emerging from the image plane into separate beams. The resolution of the system is such that a cw beam of 1 MHz produces a diffraction

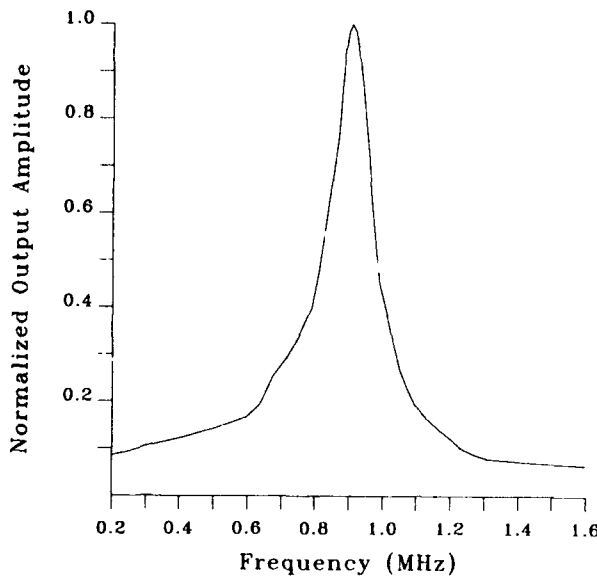


FIG. 2. Optically measured response function of a nominal 1-MHz transducer, normalized to the peak output amplitude.

pattern at the screen with an order separation of 12 cm.

Light-intensity measurements are performed with a photomultiplier tube detector positioned at the screen. A computer-controlled data-acquisition system rotates a flat mirror, passing a diffraction pattern across a slit that opens onto the detector tube element. Possible random system fluctuations can influence the acquisition of data during a single pass of a light pattern. Therefore, the computer scans a single pattern three to five times, averages, normalizes to the peak light intensity, and stores the data in a disk file. The one computer fully manages experimental input, procedure, and output, which consists of digitized diffraction patterns.

II. INITIAL PULSE ANALYSIS

The optical system is first used to model ultrasonic pulses prior to any significant harmonic distortion by nonlinear propagation.¹⁰ The construction of pulse spectra is based on an empirical model of transducer response to cw excitation. The data-acquisition system is programmed to send monochromatic signals to the transducer, which results in Raman-Nath diffraction patterns. The experimental system digitizes light patterns of m diffraction orders and converts their relative intensities I_m into values of the Raman-Nath parameter ν by the expression²

$$I_m = [J_m(\nu)]^2 \quad (1)$$

where J_m is the Bessel function of order m . The value of ν is proportional to the acoustic output amplitude of the transducer, that is its response. While keeping amplitude of the electronic signal input to the transducer constant, the data-acquisition and control system increments the frequency f and determines $\nu(f)$ across the nominal bandwidth of the transducer. The resulting transducer amplitude response as a normalized function of f is shown in Fig. 2.

The function generator introduces ideal electronic signals to the transducer system that are characterized by burst number (a positive integer describing pulse width), and pulse center and repetition frequencies f_0 and f_p , respectively. Figure 3(a) illustrates the ideal pulse time history along with its Fourier amplitude spectrum for $f_0 = 0.988$ MHz, $f_p = 66.0$ kHz, and burst number 5.

A model of the pulse train at the source within the liquid is constructed by a discrete convolution of the ideal pulse amplitude spectrum with the transfer function of Fig. 2. Since light diffraction by cw ultrasonic beams yields no information relating to pulse-phase spectra, the convolved amplitude spectrum is combined with the original ideal phase spectrum, which assumes that no phase distortion is introduced to the amplitude spectrum by the transducer system. The resulting pulse time history and convolved amplitude spectrum are shown in Fig. 3(b).

The validity of the pulse model is demonstrated by using it for input to the light-diffraction model⁸ and comparing the predicted diffraction pattern to the measured diffraction pattern produced by the actual pulse train in the liquid. For the theoretical prediction by the model, ν is now considered proportional to the pulse peak amplitude. The input for the model is expressed as a Fourier sine expansion:

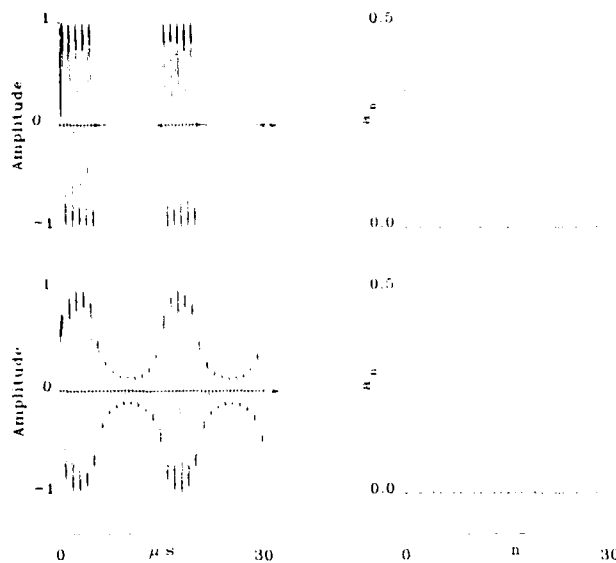


FIG. 3. Ideal pulse generator output time history with amplitude spectrum for $f_p = 66.0 \text{ kHz}$, $f_0 = 0.988 \text{ MHz}$, burst 5 (top), and the time history and amplitude spectrum after convolution with the response function of Fig. 2 (bottom).

$$v(x,t) = v \sum_{n=0}^{\infty} a_n \sin[n(\omega_p t - k_p x) + \phi_n], \quad (2)$$

where $\omega_p = 2\pi f_p$, $k_p = 2\pi/\lambda_p$, and λ_p = the pulse length in the medium. The a_n and ϕ_n are, respectively, the amplitude and phase of the n th Fourier component of the pulse. The farfield light intensity distribution as a function of diffraction angle θ is given by

$$I(\theta) = \sum_{m=-\infty}^{\infty} I_m \left(\frac{\sin(k \sin \theta - mk_p)}{(k \sin \theta - mk_p)} \right)^2, \quad (3)$$

with $k = 2\pi/\lambda$,

$$I_m = \left| \sum_{r_1=-\infty}^{\infty} \cdots \sum_{r_n=-\infty}^{\infty} J_{r_1(m)}(v_1) \cdots J_{r_n}(v_n) \cdots \exp[i[r_1(m)\phi_1 + \cdots + r_n\phi_n + \cdots]] \right|^2, \quad (4)$$

$v_n = va_n$, and $r_1(m) = m - 2r_2 - \cdots - nr_n - \cdots$.

Equation (3) represents a set of discrete diffraction orders each with an individual distribution described by the $[\sin X/X]^2$ term which is maximum when

$$\sin \theta_m = \pm m\lambda / \lambda_p. \quad (5)$$

For small pulse amplitudes, Eq. (4) reduces to $I_0 \approx 1$, and

$$I_{\pm n} \approx \frac{1}{4}(va_n)^2. \quad (6)$$

Equations (5) and (6) relate the dominant terms of the pulse amplitude spectrum directly to individual diffraction orders. For values of $v < 2$, Eq. (6) provides a direct estimate of a_n from the measured intensity I_n . Figure 4 shows the digitized pattern and resulting prediction of the pulse spectrum and light-diffraction models where good agreement is seen in all parts of the light pattern.

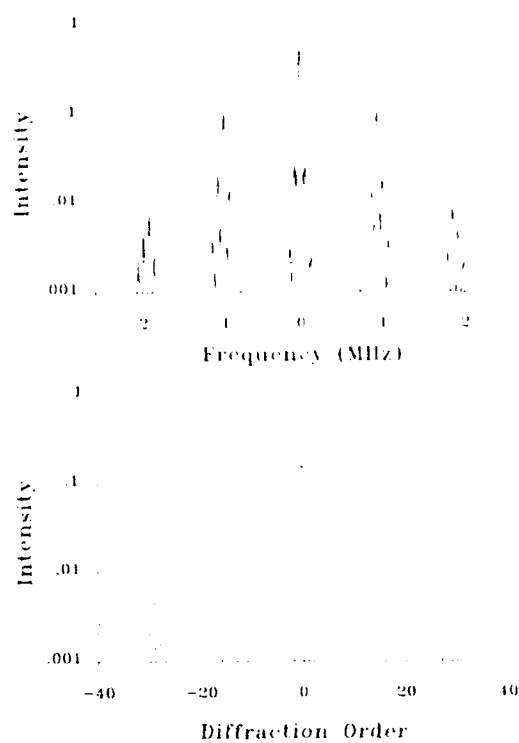


FIG. 4. Measured (top) and modeled (bottom) light-diffraction patterns produced by the pulsed beam of Fig. 3 with $v = 1.60$.

III. NONLINEAR PULSE PROPAGATION

Mayer and Neighbors⁹ calculate nonlinear propagation of pulses with a model presented by Haran and Cook.¹¹ Based on Burgers' equation, the model describes wave profile distortion as the pulse propagates along the x direction, including arbitrary frequency-dependent attenuation and harmonic generation. The one-dimensional Burgers' equation expresses the differential change of the n th harmonic component of the particle velocity U :

$$\frac{\partial U}{\partial x} = \left(\frac{\beta \omega}{c^2} \right) U \left(\frac{\partial U}{\partial \tau} \right) + \alpha \left(\frac{\partial^2 U}{\partial \tau^2} \right), \quad (7)$$

where c is the small signal-sound velocity, $\tau = t - (x/c)$ is the retarded time, α the medium attenuation coefficient, and $\beta = 1 + (B/2A)$ is the nonlinearity parameter. Expanding U in a Taylor series and combining terms up to first order with Eq. (7), Cook and Haran derive

$$U_n(x + dx) = U_n(x) + \left[\left(\frac{i\beta\omega}{c^2} \right) \left(\sum_{j=1}^r j U_j U_{n-j} + \sum_{j=n+1}^{\infty} n U_j U_{n-j}^* \right) - \alpha n^2 U_n \right] dx. \quad (8)$$

Equation (8) gives the incremental change of an acoustic wave's spectral components, where dx is the incremental distance and $*$ refers to the complex conjugate.

As input, the propagation model is given a pulse spectrum, modeled with an exponential rise and decay, along with a set of medium constants and initial conditions. The pulse has $f_0 = 2.0 \text{ MHz}$, $f_p = 125.0 \text{ kHz}$, and a rise and de-

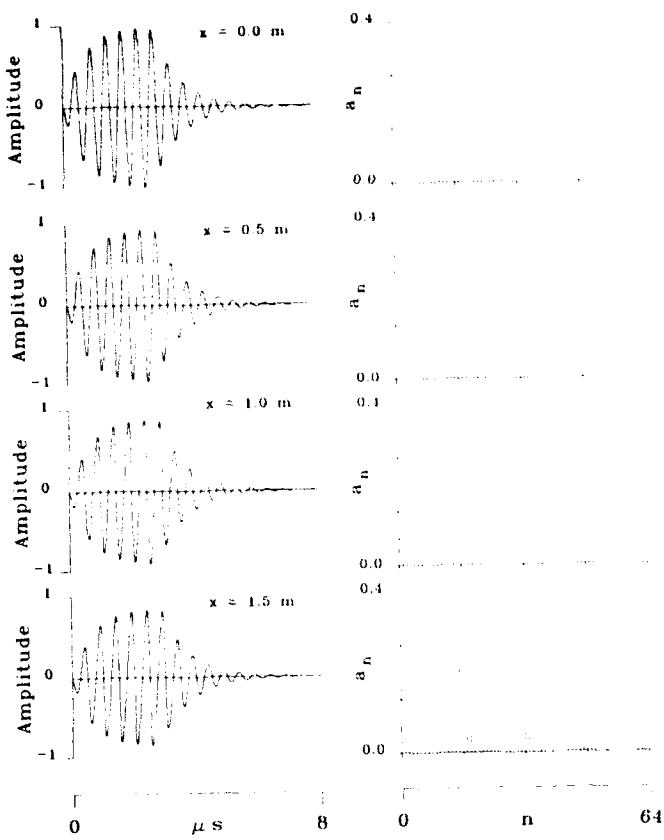


FIG. 5. A finite amplitude pulse of $f_0 = 2 \text{ MHz}$, $f_i = 125 \text{ kHz}$, and an exponential rise and decay time of $0.85 \mu\text{s}$. Medium parameters are $\alpha = \alpha'f^2$, $\alpha' = 1.9 \times 10^{-14} \text{ Np s}^2/\text{m}$, $B/A = 5.5$, $c = 1492 \text{ m/s}$, and initial amplitude $u_0 = 3 \text{ cm/s}$.

decay time of $0.85 \mu\text{s}$. The medium constants used for this example are $B/A = 5.5$, $c = 1492 \text{ m/s}$, and a quadratic frequency dependent attenuation, $\alpha = \alpha'f^2$, where $\alpha' = 1.9 \times 10^{-14} \text{ Np s}^2/\text{m}$. The initial condition consists of a 3 cm/s peak particle velocity u_0 . Figure 5 illustrates the model output, with the pulse time history and amplitude spectrum, normalized to u_0 , at four points of propagation. This illustrates the expected harmonic generation and the associated shock-front formation in each cycle of the pulse. Also indicated is the overall decrease of the pulse amplitude by attenuation.

To compare the model to an actual case of pulse propagation, an initial particle velocity u_0 must be assigned to the

TABLE I. Peak amplitude values for the pulse of Fig. 3 extrapolated from known parameters at $x = 4.5 \text{ cm}$ using Eq. (9).

$x \text{ (cm)}$	$\Phi \text{ (mV)}$	ν	$u_0 \text{ (cm/s)}$
4.5	81.6	1.60	3.12
10.0	69.6	1.35	2.25
20.0	76.4	1.35	2.46
30.0	88.4	1.35	2.85
40.0	101.9	1.35	3.29

TABLE II. Measured characteristics for water.

$c = 1487.9 \text{ m/s}$ ($T = 22^\circ \text{C}$) ^a
$B/A = 5.2^b$
$\alpha = \alpha'f^2$, $\alpha' = 2.5 \times 10^{-14} \text{ Np s}^2/\text{m}^c$

^aH. Medwin, J. Acoust. Soc. Am. **58**, 1318 (1975).

^bH. A. Kashkooli, P. J. Dolan, Jr., and C. W. Smith, J. Acoust. Soc. Am. **82**, 2086 (1987).

^cJ. M. M. Pinkerton, Nature **160**, 128 (1947).

pulse. Zankel and Hiedemann reference an expression¹² that relates u_0 to ν and the width of the ultrasonic beam, D . From Schlieren images, a D is estimated and provides $u_0 = 3.12 \text{ cm/s}$ for the pulse shown in Fig. 3. The optical beam, of 9-cm width, is assumed to sample the ultrasonic field at $x = 4.5 \text{ cm}$, the distance from the transducer face to the midpoint of the sound path through the light-ultrasound interaction region.

The Schlieren method of estimating D is acceptable near the ultrasonic source, but elsewhere is not accurate due to beam divergence. However, the beamwidth is considered by each value of ν . Also, u_0 is linearly related to the input voltage Φ to the transducer system. These two points are summarized in the relation

$$u_0 = \Gamma \Phi \nu, \quad (9)$$

where Γ is an experimental constant determined from initial conditions.

As an example, the pulse of Fig. 3 is propagated while keeping ν constant for $x > 4.5 \text{ cm}$. Appropriate values of u_0 are extrapolated from initial pulse parameters using Eq. (9) and listed in Table I. The medium constants used for water are given in Table II. The pulse spectrum and the values of Tables I and II are used for input to the propagation model. The predicted pulse amplitude spectrum shown in Fig. 6 illustrates the expected harmonic growth at 10, 20, 30, and 40 cm from the transducer.

The level of harmonic distortion shown in Fig. 6 is small compared to the example of Fig. 5 since the total propagation distance is smaller. This low level of distortion presents no problem for this investigation due to the diffraction pattern's extreme sensitivity to pulse shape. The propagated pulse spectra are used for input to the diffraction model for comparison to actual light patterns.

Experimental pulse propagation is performed with the optical system by positioning the transducer, within the interaction vessel, at selected distances away from the axis of the collimated light beam. Once the transducer is fixed at the desired distance, the data-acquisition system performs the experiment and stores the resulting digitized diffraction pattern. The measured patterns and the diffraction model output are shown in Fig. 7.

Analogous to the results of Zankel and Hiedemann⁴ for cw ultrasonic beams, the asymmetry of the diffraction orders about I_0 can be seen in both the measured and modeled pulse light patterns. The growth of the first set of pulse harmonics is indicated in the diffraction orders about $I_{2 \text{ MHz}}$ (I_{28}), which, due to a phase shift, appears as a decrease in the diffraction orders about $I_{-2 \text{ MHz}}$ (I_{-28}).

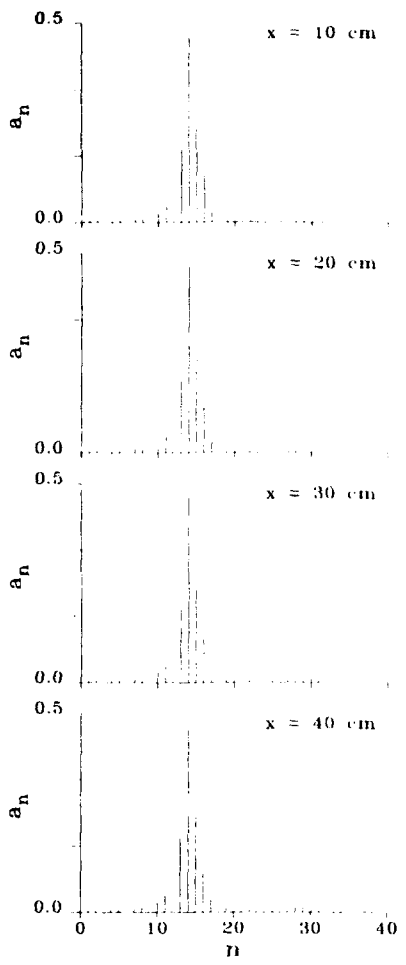


FIG. 6. Pulse spectrum of Fig. 3 at four stages of propagation for u_0 and medium constants as listed in Tables I and II.

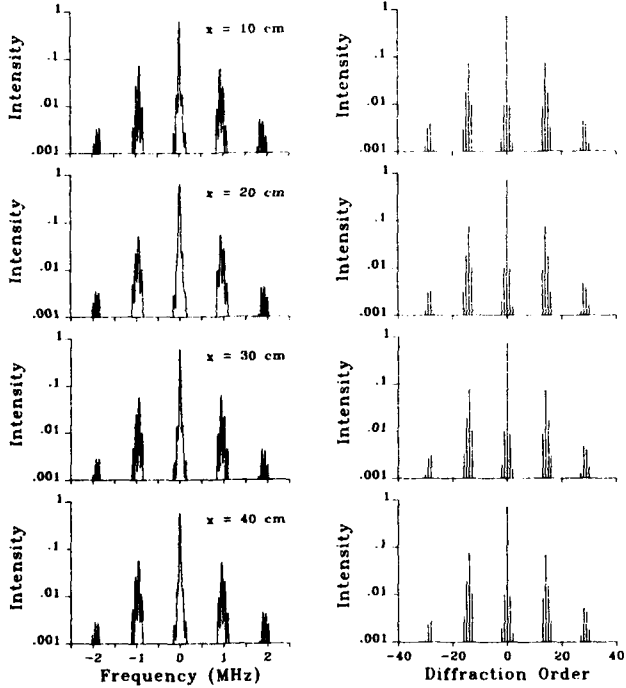


FIG. 7. Measured (left) and modeled (right) light-diffraction patterns produced by the pulsed beam spectra of Fig. 6 each with $v = 1.35$.

TABLE III. Peak amplitude values for a pulse of $f_p = 122.0 \text{ kHz}$, $f_0 = 0.987 \text{ MHz}$, and burst number 3.

x (cm)	Φ (mV)	v	u_0 (cm/s)
40.0	73.4	0.81	1.80
40.0	100.0	1.11	2.46
40.0	126.7	1.41	3.12

As another example, a pulse of different spectral content is propagated and analyzed optically. The pulse is sampled repeatedly at $x = 40 \text{ cm}$; however, in this case the initial amplitude u_0 is varied. Since the same ultrasonic source is used, a pulse spectrum is generated using the response curve of Fig. 2, but with values $f_p = 122.0 \text{ kHz}$, $f_0 = 0.987 \text{ MHz}$, and burst number 3. The constants of Table II are used with values for u_0 and v summarized in Table III.

The combined output of the propagation and diffraction models are compared to measured light patterns in Fig. 8. The harmonic distortion increases with initial pulse amplitude as predicted by theory. This set of diffraction patterns illustrates the decrease of the original amplitude terms due to the transfer of their energy to the first set of pulse harmonics. Both examples illustrate good agreement between measurement and theory, as well as the sensitivity of optical analysis to even subtle harmonic distortions of pulsed ultrasonic fields.

IV. CONCLUSIONS

The results presented here demonstrate the applicability of light diffraction to an analysis of ultrasonic pulses in a nonlinear medium. With the pulse modeling provided by preliminary diffraction studies, a pulse spectrum has been constructed for input to the propagation model of Haran and

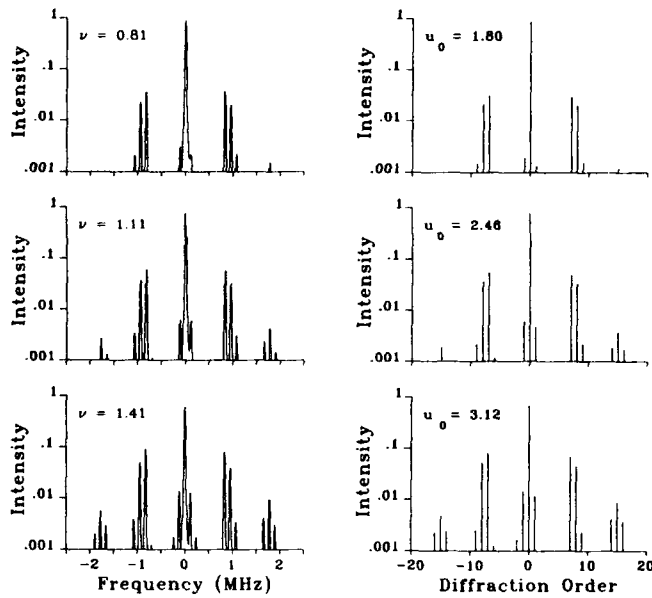


FIG. 8. Measured (left) and modeled (right) light-diffraction patterns for medium constants and pulse values as listed in Tables II and III.

Cook.¹¹ The predictions of the propagation model, when used with the diffraction algorithm, show good agreement with light patterns measured by the experimental apparatus. Although very subtle for small propagation distances, pulse harmonic distortion produces an observable asymmetry in light-diffraction patterns. These results support the suggestion of Mayer and Neighbors⁹ that an estimate of pulse harmonic growth can be attained by a study of light-diffraction patterns.

ACKNOWLEDGMENT

This work was supported by the Office of Naval Research, U.S. Navy.

- ¹R. Lucas and P. Biquard, C. R. Acad. Sci. (Paris) **195**, 121 (1932).
- ²P. Debye and F. W. Sears, Proc. Natl. Acad. Sci. USA **18**, 63 (1932).
- ³C. V. Raman and N. S. N. Nath, Proc. Ind. Acad. Sci. A **2**, 406-412 (1935).
- ⁴K. L. Zankel and E. A. Hiedemann, J. Acoust. Soc. Am. **31**, 44-54 (1959).
- ⁵L. E. Hargrove, J. Acoust. Soc. Am. **43**, 847 (1968).
- ⁶R. N. Zitter, J. Acoust. Soc. Am. **43**, 864 (1968).
- ⁷E. Hausler, W. G. Mayer, and M. Schwartz, Acoust. Lett. **4**, 180 (1981).
- ⁸T. H. Neighbors, III and W. G. Mayer, J. Acoust. Soc. Am. **74**, 146-152 (1983).
- ⁹W. G. Mayer and T. H. Neighbors, III, Ultrasonics **25**, 83-86 (1987).
- ¹⁰J. Wolf, T. H. Neighbors, III, and W. G. Mayer, Ultrasonics **27**, 150-154 (1989).
- ¹¹M. E. Haran and B. D. Cook, J. Acoust. Soc. Am. **73**, 774-779 (1983).
- ¹²G. W. Willard, J. Acoust. Soc. Am. **21**, 101-108 (1949).